Multi-source Energy Harvesting for Wildlife Tracking

You Wu

Thesis submitted to the faculty of the Virginia Polytechnic Institute and State University in partial fulfillment of the requirements for the degree of

Master of Science

In

Mechanical Engineering

Lei Zuo, Chair

Robert G. Parker

Steve C. Southward

May 11, 2015

Blacksburg, VA

Keyword: Multi-source energy harvester, wildlife tracking, solar energy harvester, Maximum Power Point Tracking, broadband electromagnetic energy harvester, Mechanical Motion Rectifier (MMR)

Multi-source Energy Harvesting for Wildlife Tracking

You Wu

ABSTRACT

Sufficient power supply to run GPS machinery and transmit data on a long-term basis remains to be the key challenge for wildlife tracking technology. Traditional ways of replacing battery periodically is not only time and money consuming but also dangerous to live-trapping wild animals. In this paper, an innovative wildlife tracking collar with multi-source energy harvester with advantage of high efficiency and reliability is proposed. This multi-source energy harvester entails a solar energy harvester and an innovative rotational electromagnetic energy harvester is mounted on the "wildlife tracking collar" which will extend the duration of wild life tracking by 20% time as was estimated. A feedforward and feedback control of DC-DC converter circuit is adopted to passively realize the Maximum Power Point Tracking (MPPT) logic for the solar energy harvester. A novel electromagnetic pendulum energy harvester with motion regulator is proposed which can mechanically rectify the irregular bidirectional swing motion of the pendulum into unidirectional rotational motion of the motor. No electrical rectifier is needed and voltage drops from diodes can be avoided, the EM pendulum energy harvester can provide 200~300 mW under the 0.4g base excitation of 4.5 Hz. The nonlinearity of the disengage mechanism in the pendulum energy harvester will lead to a broad bandwidth frequency response. Simulation results shows the broadband advantage of the proposed energy harvester and experiment results verified that at some frequencies over the natural frequency the efficiency is increased.

Acknowledgements

I would like to thank Dr. Lei Zuo, Dr. Robert G. Parker and Dr. Steve C. Southward to serve as my committee member and guide me during my master's study in Virginia Tech.

I would like to express my sincere gratitude to everyone who helped and supported me during my study in both Stony Brook University and Virginia Tech. I would not be able to accomplish this work without them.

I would like to express my deep thanks to my advisor, Dr. Lei Zuo, for his guidance and cultivation since the first day I joined this group. He is a smart, rigorous and knowledgeable scholar and the most hardworking person I have ever seen. He spends almost all time working on projects and proposals except for some very limited sleeping time. He is very conscientious and explore deep in research. He has a very good scientific sense on academic problems and gave me many constructive and valuable instructions during my study. I really learned a lot from him.

I would like to thank Mr. George Luhrs in Stony Brook and Mr. James Dowdy in Virginia Tech for their help on experiment.

I would like to thank my lab mates Changwei Liang, Yilun Liu, Peng Li, Shaoxu Xing, Hongbo Yu, Junxiao Ai, Gaosheng Fu, Xiudong Tang, for helping me on my study.

I would like to thank my wife Wanlu Zhou, for her countless help and accompany on both my research and daily life.

At last, I would like to thank my family. Their support and devotion make my life better.

Table of Contents

List of Figures

List of Tables

1. Introduction

1.1. Background and motivation

Wildlife tracking technology has been greatly expanded for ecology studying in the past several decades, it has greatly extended our ability to study the ecology of wild animals in natural environments, from marine to terrestrial environments [1, 2]. Battery-powered electronics embedded in backpacks, collars, implants and other forms of animal attachment can record the physical location and activity of animals, aspects of their immediate environment (such as temperature and humidity), and even aspects of their physical condition through biotelemetry. These devices can transmit data to researchers in real time through the satellite-based ARGOS/GPS system or GSM phone network [3].

Despite tremendous technological advances combined with significant miniaturization of components (enabling ever-smaller animals to be monitored), sufficient power to run the complex GPS machinery and store and transmit data under inclement and widely variable temperature regimes remains the key limiting factor for the questions ecologists can ask using these technologies.

There remains a fundamental tradeoff in the duration and intensity of animal monitoring such that we can get frequent animal locations over short periods of time (which isn't terribly useful for long-lived species) or infrequent data (significantly less resolution in terms of animal behavior) over longer time frames. Moreover, the cost of these devices isn't trivial and retrieving the devices for redeployment on additional animals or replace the batteries to increase statistical sample size is a common desire although rather tricky in practice either due to the large cost and danger of live-trapping wild animals or the high failure rate of remote "drop-off" buckles affixed to GPS collars. Common ways to recapture the animals, in example helicopter darting and barrel traps, anesthetic drugs and leg hold snares, are either very expensive, approximately $1,000 per capture, or time consuming and can be very lethal to animals [4, 5]. The needs for alternative means of supplying power, so as to enable high-frequency locations on animals with over ever longer time frames, is the motivating force behind this thesis.

1.2. Review on the small scale energy harvesting

The wildlife tracking unit must be very lightweight to avoid interfering with the animal's everyday life and also long duration and high monitoring intensity are the desired for these devices. Therefore, light weight tracking unit plus the light weight power supply and small scale energy harvester is required to achieve these goal. Photovoltaic, piezoelectric, electromagnetic and electrostatic are commonly used ways for energy harvesting. Most piezoelectric electricity sources produce power on the order of mill watts, it's too small for system application and have very low power to weight ratio. Electrostatic energy harvesting is based on the changing capacitance of vibration-dependent capacitors, it requires pre-charge on the devices which is not applicable on wildlife tracking usage. Therefore, solar energy harvesting and electromagnetic energy harvesting methods and research are investigated in this section.

1.2.1. Solar energy harvester

Due to the environmental issue and global energy crisis, the renewable, no noise solar energy harvester is becoming more important these days. Solar panels are usually modeled as a voltage limited current source and its output voltage is related with ambient light intensity, temperature and load. The Maximum Power Point (MPP) for a solar panel, shown in figure 1-1 and 1-2 [6], is a single operating point on the IV curve of a solar panel where the values of the current times voltage of the cell result in a maximum power output under certain ambient light intensity [7]. Therefore it is very imperative to track the Maximum Power Point of a solar energy harvester to maximize its power output.

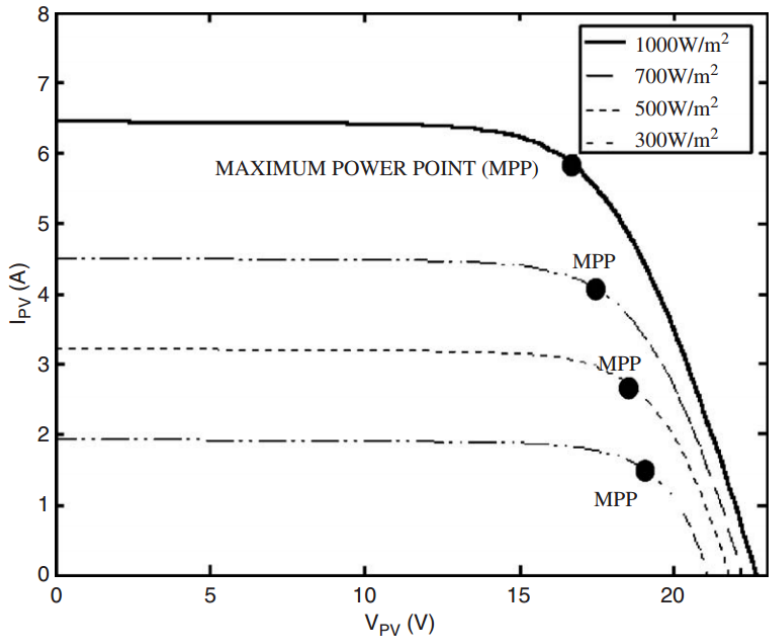

Figure 1-1 I– V photovoltaic characteristic for four different irradiation levels [6]. Salas, V., et al., Review of the maximum power point tracking algorithms for stand-alone photovoltaic systems. Solar Energy Materials and Solar Cells, 2006. 90(11): p. 1555-1578. Used under fair use, 2015.

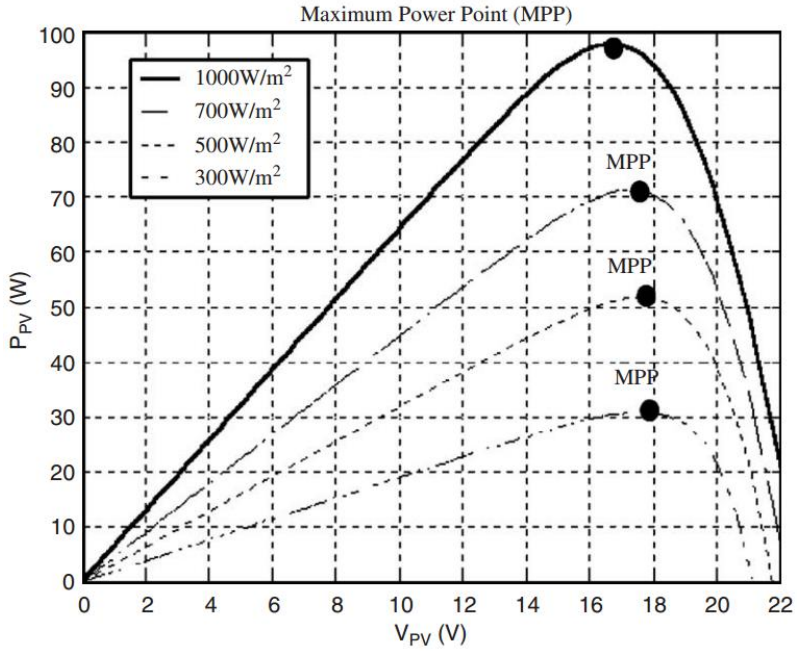

Figure 1-2 P– V photovoltaic characteristic for four different irradiation levels [6]. Salas, V., et al., Review of the maximum power point tracking algorithms for stand-alone photovoltaic systems. Solar Energy Materials and Solar Cells, 2006. 90(11): p. 1555-1578. Used under fair use, 2015

There are various methods for maximum power point tracking. Some researchers used curve-fitting technique [8-11] that numerically approximate the MPPT tracking, this method can

calculate the voltage at MPP and adjust the loading in a short time however is not accurate. Some papers [12-14] calculated the MPP of the solar panel system before hand for different environmental conditions and stored these data in the memory of MPPT control system. During operation, the controller will look up the table of the stored date for the current environmental condition to achieve the MPP tracking. This method can be very accurate for application however it requires lots of work in advance for calibration. Perturbation and Observation (P&O) method [15-18] is commonly used in practice for MPPT tracking. This method doesn't require a previous knowledge of solar generator characteristics however it requires a complex algorithm and it has negative effects from its drawback. Femia, Nicola, etc. [19] showed that the P&O MPPT algorithm must be customized to the dynamic behavior of the specific converter in order to limit its negative effects. [20-23] addressed several MPPT methods used for real application.

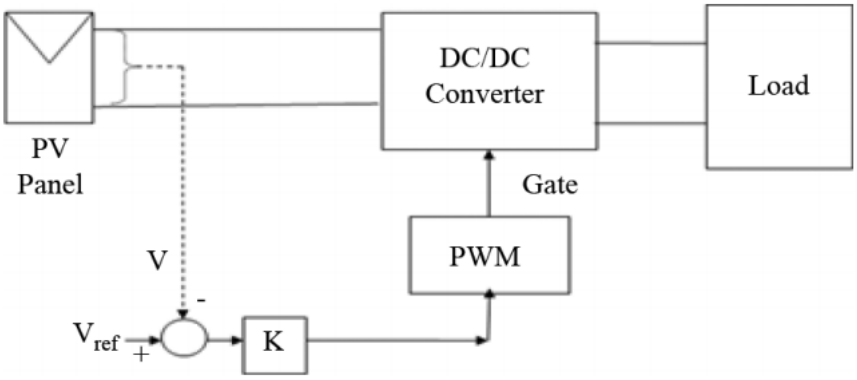

Figure 1-3 Voltage-feedback with PWM modulation [24]. Subudhi, B. and R. Pradhan, A Comparative Study on Maximum Power Point Tracking Techniques for Photovoltaic Power Systems. Ieee Transactions on Sustainable Energy, 2013. 4(1): p. 89-98. Used under fair use, 2015

The methods listed above require complex algorithm and a microcontroller or microprocessor in order to implement this control method for MPPT. Some methods [25-28] use voltage or current from the solar panel as feedback and simple control method to achieve autonomous MPPT. The algorithm of voltage based feedback control with PWM modulation [24] is shown in figure 1-3. The voltage output from the PV panel is used to control the gate of DC-DC converter which can adjust the voltage output from the PV panel to MPP. Different V_{ref} and K values will be adjusted for different PV panels. This method might not be accurate as the ones listed above with complicate control but doesn't require microcontroller to achieve MPPT, it is often used if no battery is presented in the system.

Inspired by the feedback control methods used in solar panel MPPT and the widely used feed-forward and feed-backward method in control area, a feedforward and feedback control of a dc-dc boost converter based MPPT algorithm is proposed in this thesis.

1.2.2. Electromagnetic energy harvester

Electromagnetic energy harvester is a type of energy harvester utilizing electromagnetic effect to generate electrical energy. It is always comprised of magnets and coils. Mechanical vibration may induce relative movement of these magnets and coils, so that the mechanical vibration energy can be converted into electrical energy.

Many studies have been done on the design and analysis of the electromagnetic energy harvester. Arian Rahimi, et al. [29] presented a vibration-based compact electromagnetic energy harvester. A high efficiency full-wave interface rectifier electronics is implemented to achieve DC output from the energy harvester. Shad Roundy [30] et al. developed a planar electromagnetic energy harvesting transducer which uses low cost printed circuit board and multi-pole magnetic sheets, figure 1-4. A detailed analytical model is developed and the device can achieve an efficiency of 9%.

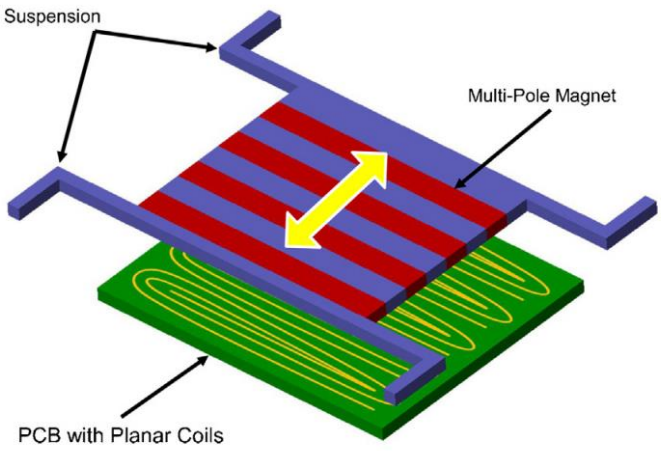

Figure 1-4 Schematic of basic transducer concept [30]. Roundy, S. and E. Takahashi, A planar electromagnetic energy harvesting transducer using a multi-pole magnetic plate. Sensors and Actuators a-Physical, 2013. ***195****: p. 98-104. Used under fair use, 2015.*

Arian Rahimi, et al. [31] proposed a compact energy harvesting system with an electromagnetic generator and AC-DC converter with frequency up-conversion technique. An electromagnetic energy harvester to harvest energy from vibration induced by Kármán vortex

street is demonstrated by Dung-An Wang, et al. [32]. Rohan Dayal, et al[33] introduced a low-voltage electromagnetic energy harvesting systems with a microgenerator and AC-DC power processing circuit. Zorlu, et al. [34] presented a vibration-based electromagnetic energy harvester using a mechanical frequency up-conversion method for harvesting energy in low frequency. An electromechanical power generator to convert vibrations to electrical energy with electromagnetic transducer is proposed by Marioli D, et al[35], figure 1-5.

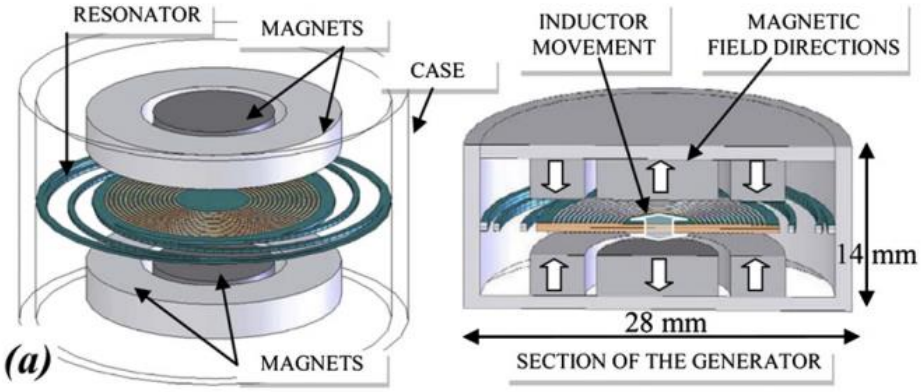

Figure 1-5 The electromagnetic generator (left) and its cross section (right) [35]. D, M., S. E, and S. M, Electromagnetic generators employing planar inductors for autonomous sensor applications. Procedia Chemistry, 2009(1:4): p. 69-72. Used under fair use, 2015.

The vibration-based energy harvesters presented above are designed as linear resonators to achieve optimal performance by matching their resonance frequencies with the excitation frequencies. However, a slight shift of the excitation frequency will cause a dramatic reduction in power generation [36]. Therefore, broadband energy harvesting has attracted more and more attention in recent years.

Many researchers used nonlinearity to enhance the performance of vibration-based energy harvesters. Nonlinear energy harvesting devices have been shown to be capable of harvesting energy in wider frequency ranges delivering more power than their linear counterparts. Yang, et al. [37] proposed a multi-frequency energy harvester which consists of three permanent magnets, three sets of two-layer copper coils and a supported beam. Lei Gu, et al. [38] presented a passive self-tuning energy harvester for rotational vibration applications. The experiment demonstrated significantly improved performance compared with untuned harvester, figure 1-6.

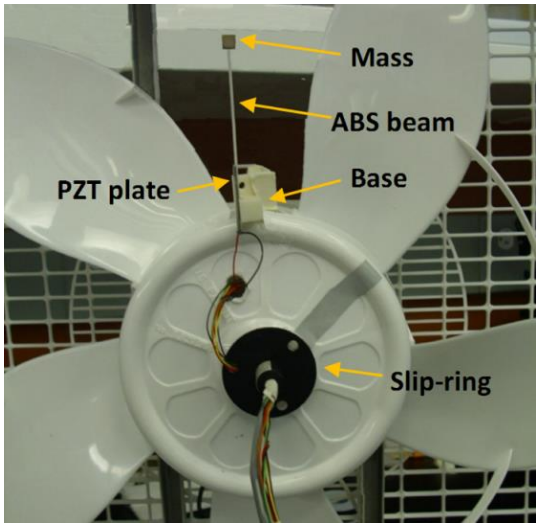

Figure 1-6 Experimental setup for harvesting energy from rotational[38]. Gu, L. and C. Livermore, Passive self-tuning energy harvester for extracting energy from rotational motion. Applied Physics Letters, 2010. ***97****(8). Used under fair use, 2015.*

Stanton, et al. [39]designed a nonlinear energy harvester capable of bidirectional hysteresis, which performs a broadband energy harvesting ability by tuning nonlinear magnetic interactions around the end mass. They also presented another design of a bi-stable inertial oscillator comprised of permanent magnets and a piezoelectric cantilever beam[40]. Ferrari, et al. [41]investigated the energy harvesting performance of the same kind of bi-stable energy harvester under white-noise excitation. Vinod R Challa, et al. [42] presented a vibration energy harvesting device with autonomous resonance frequency tunability utilizing a magnetic stiffness technique, figure 1-7. This device is successfully tuned from −27% to +22% of its untuned resonance frequency.

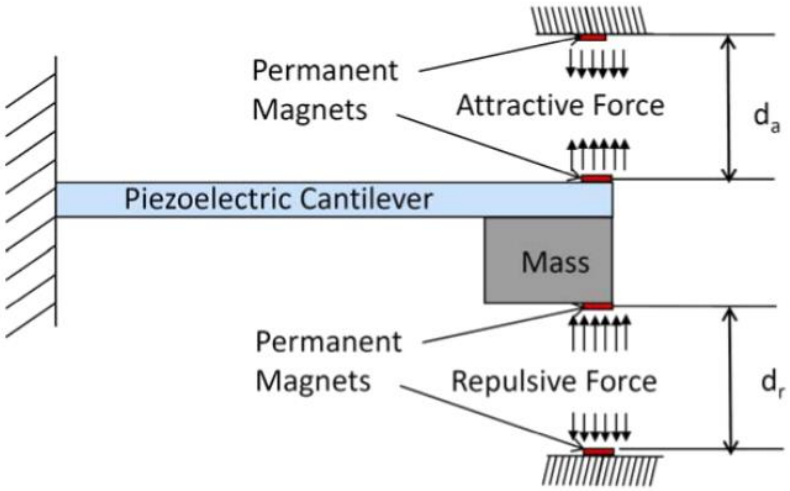

Figure 1-7 Schematic of the variable magnetic stiffness resonant [42]. Challa, V.R., M.G. Prasad, and F.T. Fisher, Towards an autonomous self-tuning vibration energy harvesting device for wireless sensor network applications. Smart Materials & Structures, 2011. ***20****(2). Used under fair use, 2015.*

Arrieta, et al. [43]proposed a bi-stable composite plate with bonded piezoelectric patches for broadband nonlinear energy harvesting. Mann and Sims [44]designed a nonlinear energy harvester using magnetic forces to levitate an oscillating center magnet with a tunable resonance. Mann and Owens [45]investigated a nonlinear energy harvester that uses magnetic interactions to create an inertial generator with a bi-stable potential well.

Among the various kinds of vibrations, pendulum-like vibration is a type of widely existing vibration. Quite a few research has been done on pendulum energy harvesting technology. A well-weighted pendulum for energy harvesting from a rotating wheel, consisted of a pendulum and one or more weights, is able to adjust its natural frequency to meet the wheel rotation frequency[46]. Cottone, et al. [47]investigated a piezoelectric inverted pendulum energy harvester, where on top of the pendulum mass a small magnet is added. The excitation is generated by a properly designed magnetic excitation on two small magnets attached near the base of the pendulum. While the pendulum oscillates, the piezoelectric beam is bended and thus generates electrical energy. Mitcheson, et al. [48]presented a power electronic interface that is capable of continual adjustment of the damping and resonant frequency of a pendulum energy harvester, which is designed for harvesting energy from the rocking motion in a small boat.

In conclusion, the nonlinearity enhanced energy harvester can harvest energy over a broader bandwidth than those linear oscillator based single degree of freedom energy since they

are not sensitive to the change of external source frequency. And an AC-to-DC converter is required to rectify the AC voltage output from these energy harvesters into a DC source in order to store the energy, how to reduce the power consumption and voltage drop during rectification processing remains a key problem to improve the efficiency of the vibration based electromagnetic energy harvester.

In this thesis, a nonlinear mechanical motion rectifier based electromagnetic pendulum energy harvester is proposed. Based on the property of roller/one-way clutch, the energy harvester can mechanically rectify the bidirectional swing motion of the pendulum into unidirectional rotational motion of the motor to achieve a DC output. Due to the nonlinearity of one-way clutch, it can also achieve a broader bandwidth performance.

1.3. Review on the one-way clutched based mechanical system

A one-way clutch based pendulum energy harvester is proposed in this thesis, the system is essentially a switched/piecewise linear system. A rotational inertia and an electrical damping are added in and subtracted during the switch and the system is changing between a single DOF system and a two DOF system. The switching criteria is dependent on time and current state of the system. In order to analyze its property, relative works on the nonlinear dynamics of one-way clutch based switched linear system are examined.

Lau, S. L., and W-S. Zhang [49] extended the incremental harmonic balance (IHB) method to analyze the periodic vibrations of systems with a general form of piecewise-linear stiffness characteristics. Mockensturm, Eric M., et al. [50] presented a method of analysis of systems containing one-way clutches. The power transmission and the influence of large inertia elements in a serpentine belt drive system is examined. Ding, Hu, and Jean W. Zu. [51] analyzed the steady-state response of a pulley-belt system with a one-way clutch and belt bending stiffness. The four-stage Runge-Kutta algorithm is employed for time discretization of the nonlinear piecewise ordinary differential equations and the fast Fourier transform is used for obtaining the natural frequencies of the nonlinear vibration. Gill-Jeong, Cheon [52] studied the nonlinear behavior analysis of a paired spur gear system with one-way clutch and verified that a one-way clutch is effective for reducing torsional vibration. Zhu, Farong, and Robert G. Parker [53, 54] analyzed one-way clutch based two-pulley and three-pulley serpentine belt drive system. The one-way clutch is modeled as a piecewise linear spring with discontinuous stiffness which can separate the

driven pulley into two degrees of freedom. Li, Zhongjie, et al. [55] proposed a one-way clutch involved mechanical motion rectifier based energy-harvesting shock absorbers which achieved high efficiency in high frequency. Orazov, B, et al. [56] proposed a novel excitation scheme of a buoy-type ocean wave energy converters which can exhibit resonant responses at low ocean wave frequency. The system is modeled as a switched linear system. Diamond, Christopher A. et al. [57] improved the model of the switched linear wave energy converter presented in [56] by accounting the momentum transfer during switching.

1.4. Objective and Contributions of this study

In this paper, a multi-source energy harvester for wildlife tracking is presented which contains a solar energy harvester and an innovational rotational electromagnetic energy harvester. These multi-source energy harvesters can feed the power supply of GPS and greatly expand the duration of the tracking collar. A light sensor based feedforward and feedback DC-DC boost converter is demonstrated and simulated for solar energy harvester. This boost converter can passively track the Maximum Power Point without using any complicate microcontroller or DSP. An innovative broad-band pendulum energy harvester with motion regulator is proposed which has the ability of regulating the bidirectional swing motion of the pendulum into unidirectional rotational motion of the motor, so that we can avoid the voltage drop from the electrical diodes in AC-to-DC rectifier. Therefore, the efficiency of the energy harvester can be significantly improved [12]. Another important advantage of the proposed energy harvester is the integration of disengage mechanism into the system. Without disengage mechanism in traditional energy harvester, the rotational speed of the motor is limited by the swing speed of the pendulum, which will drop down when the pendulum swing over the equivalent position and start to slow down when approaching the higher location. Also single DOF system is very sensitive to the change of driving frequency, a slit shift on the driving frequency will cause a large power output drop for single DOF system. However, with disengage mechanism, the rotational speed of our proposed energy harvester can stay in a high value when the pendulum swing speed is slower than the motor speed. Thus, more electrical energy can be generated from the motor. With this advantage, the proposed energy harvester can harvest energy in a much wider frequency range, and meanwhile the disengage mechanism can protect system and harvesting energy from large impacts.

1.5. Thesis organization

This paper is organized as follows. In chapter 2, an overview of wildlife tracking collar is shown. In chapter 3, modeling and simulation for the solar energy harvester is presented. In chapter 4, an innovative broad bandwidth pendulum energy harvester is proposed, detailed design, modeling and experimental verification are illustrated. The conclusion of proposed work is presented in chapter 5.

2. Overview of wildlife tracking collar

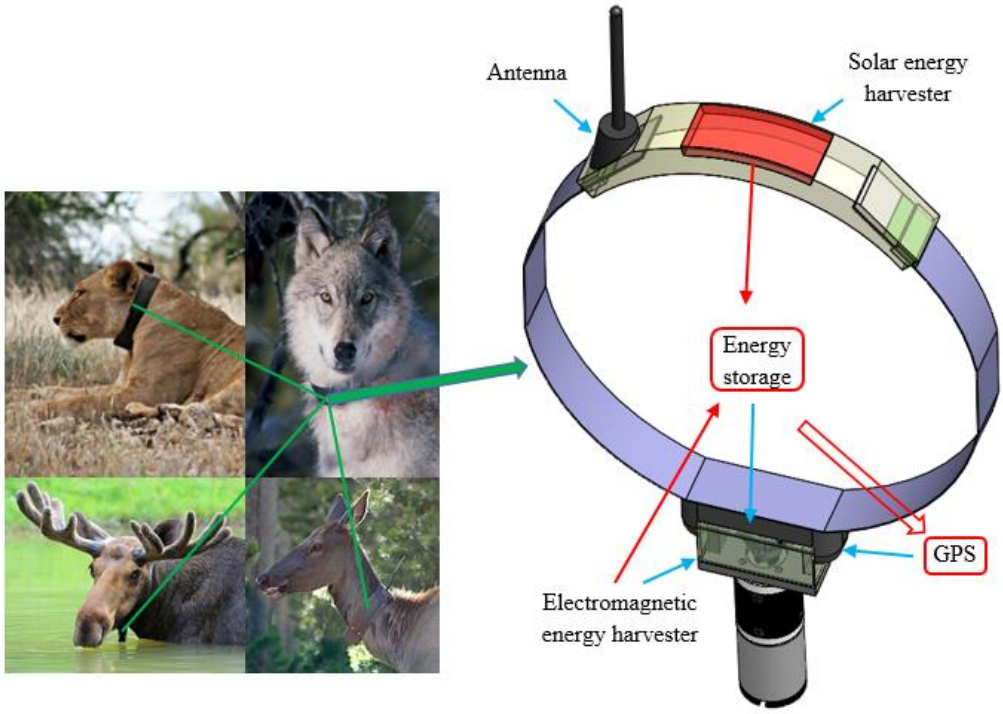

Figure 2-1 Overview of wildlife tracking collar. http://home.groundlab.cc/lioncollars.html. http://www.spokesman.com/blogs/outdoors/2013/feb/12/idaho-research-helicopter-targets-elk-moose-wolves/. http://www.salon.com/2013/07/21/minnesotas_moose_mystery_partner/. Used under fair use, 2015.

The overview of the concept for the proposed wildlife tracking collar is shown in Figure 1, which is comprised of three parts: multi-source small scale energy harvester, energy storage unit and GPS based communication unit. The multi-source energy harvester is consisted by a solar energy harvester and a rotational electromagnetic energy harvester, it is designed to provide electrical power for the GPS devices for monitoring free-ranging wild animals. The solar energy harvester can harvest energy from the ambient solar light and the electromagnetic energy harvester would harvest energy from the kinetic energy from animal's motion to generate sufficient electrical energy to power a GPS navigation device. The electrical energy is stored in the energy storage unit and can extend the duration of GPS in the wildlife tracking device.

There remains a fundamental tradeoff in the duration of the GPS and intensity of animal monitoring such that we can get frequent animal locations over short periods of time or infrequent data over longer time frames. A typical wildlife tracking device needs 200-300 mW for actively collecting locations and sending out wireless data, and micro watts when in sleep mode. On

average, 50-100 mW of energy would be enough for long term wildlife tracking (data send out per 15-20 minutes) [58]. Since the multi-source energy harvester can harvest both solar energy and mechanical motion energy, it can be applied for both slow-motion or desert animals and considerably more active animals in forest environments. The duration of the power supply system can be extended due to the implementation of multi-source energy harvester, therefore the duration and reliability of the wildlife tracking system will be significantly improved.

3. Solar Energy Harvester

Solar panel is usually treated as a voltage limited current source. This property makes it difficult to act as a power source and charge regular batteries because the output voltage of the solar panel changes along with the ambient light intensities as well as the time variance loading impedance. The I-V curve of solar panel under different sunlight intensities is shown in figure 3-1 [59], as we can see in the figure, the current output from solar panel is increased when the ambient light intensity increases since solar panel is a voltage limited current source. By changing the impedance in the circuit, the voltage output from solar panel starts increasing while the output current remains the same. However, after the voltage crossed the region marked as red dash line, the output current quickly drops since the solar panel can't provide sufficient power to maintain high voltage.

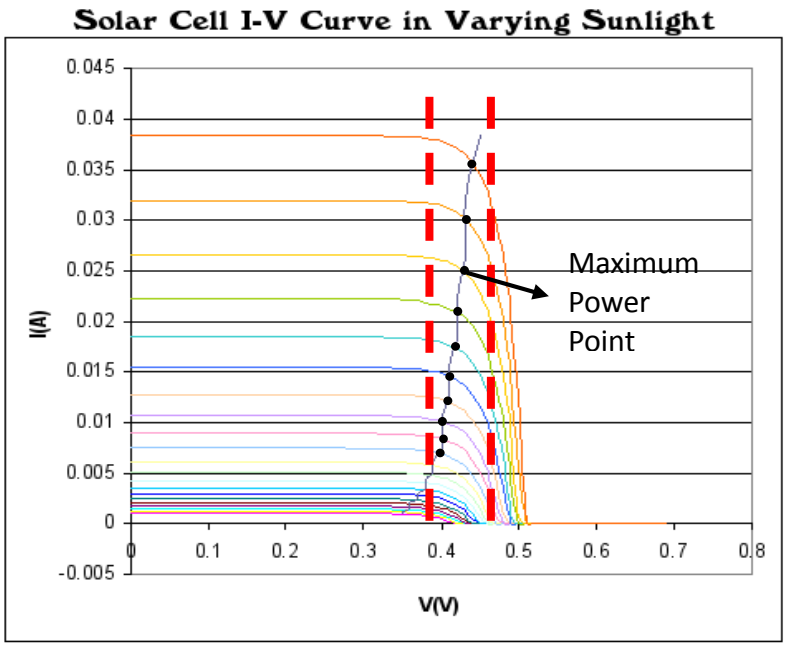

Figure 3-1 I-V curve of solar panel under different sunlight intensities[59]. ZyMOS, Solar cell current-voltage curve with the max power point indicated. Wikimedia, http://commons.wikimedia.org/wiki/File:Solar-Cell-IV-curve-with-MPP.png, 2006. Used under fair use, 2015.

The power output from the solar panel can be calculated by the area covered on the I-V curve and there is a Maximum Power Point (or MPP, marked as black dot in figure 3-1) on each curve. It represents the point on the I-V curve that maximize the power output at the given level

of light intensity. Maximum Power Point Tracking (MPPT) is necessary to increase the efficiency of solar panel.

The algorithm of MPPT method is basically detecting the environmental condition and set the loading impedance correspondingly. In a word, MPPT method can track the MPP of the solar panel and maximize the power output from the solar panel. The solid black line in the figure is an array of the Maximum Power Points (MPP) for the given solar panel. The MPP almost drops within a certain voltage range. The principle of MPPT method in this thesis is to keep the voltage output of solar panel under certain range with sufficient change in environment, such that in the desired light intensity the solar panel charge circuit can track the MPP passively without using complicated and power consumed control method, in example, MPU based MPPT method.

3.1. Feedforward and feedback control of a dc-dc boost converter for MPPT

For small solar panels that supply for the our GPS tracking system, the open circuit voltage is usually lower than the battery supply, thus a DC-DC converter is needed to boost up the voltage to a certain level in order to charge the battery.

Chulsung Park and Pai H. Chou [60] introduced a feedforward control of a DC-DC boost converter for solar panel MPPT. With the introduction of feedforward control, the boost converter can stabilize the output voltage from solar panel to maximize the efficiency of the solar energy harvester. In their paper, a light sensor is used to detect the ambient light intensity by comparing the voltage of the light sensor and the voltage from the solar panel through a comparator. A PWM signal is generated in the circuit, the duty cycle of the PWM signal will change with the change of ambient light intensity and the output voltage of solar panel is kept into a hysteresis band around MPP.

The concept of feedback and feedforward control is widely used in control area and inspired by Chulsung's paper, a feedforward and feedback control of a dc-dc boost converter method is proposed in this thesis for MPPT.

We need a feedback control for MPPT because in a long term utilizing of the solar panel based charging circuit, the voltage of the energy storage element can be variable. In order to keep

solar panel working around MPP, we need take into consideration of the energy storage element condition. A feedback control circuit is implemented into the feedforward control of DC-DC boost converter circuit, as is shown in figure 3-2.

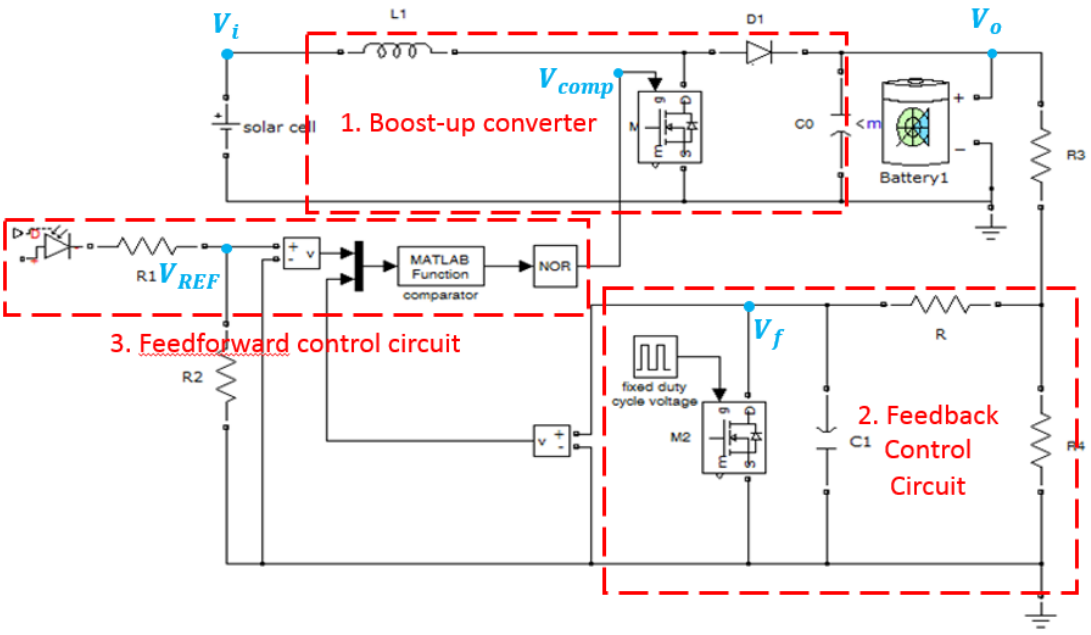

Figure 3-2 Feedforward and feedback control of a dc-dc boost converter

The feedforward and feedback control of DC-DC boost converter circuit contains three parts: a Boost converter, a feedback control circuit, and a PWM generate circuit. V_i is the input voltage of this circuit and it's also the voltage output from solar panel, V_0 is the voltage output of this circuit, V_f is the voltage output from the feedback control circuit and V_{REF} is the reference voltage from light sensor which monitored the ambient light intensity change. The function of each parts will be discussed separately in the following sections.

3.1.1. Boost-up converter circuit

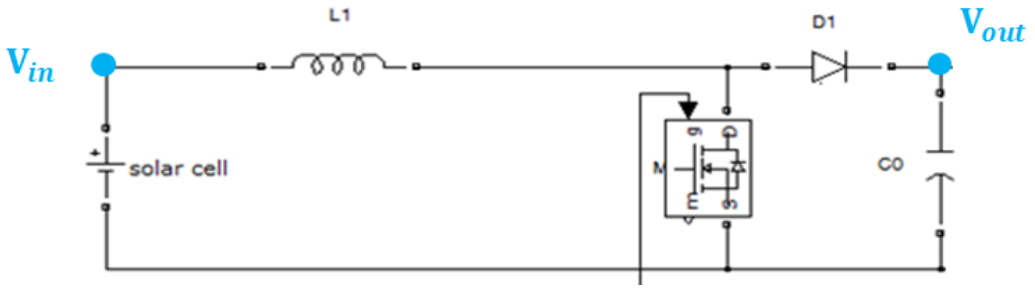

Figure 3-3 Boost converter circuit

The boost converter circuit contains 5 elements: a solar panel as a power source, an inductor L_1, a diode D_1 and a capacitor C_0. When the boost converter works in continues mode, which requires the current through the inductor L_1 never falls to zero, the output voltage of solar panel V_i and output voltage of this circuit V_o has the relationship below[61]:

$$\frac{V_{out}}{V_{in}} = \frac{1}{1-D} \tag{3.1}$$

Where D is the duty cycle of MOSFET, it represents the fraction of the commutation period T during which the switch is On. Therefore D ranges between 0 (Switch is never on) and 1 (Switch is always on). The function of this circuit is basically changing the charge and discharge time ratio of the capacitor C_0, and boost up the voltage output from solar panel/cell by $\frac{1}{1-D}$ times. By controlling the duty cycle of MOSFET, the circuit will change the output voltage V_{out}.

3.1.2. Feedback control circuit

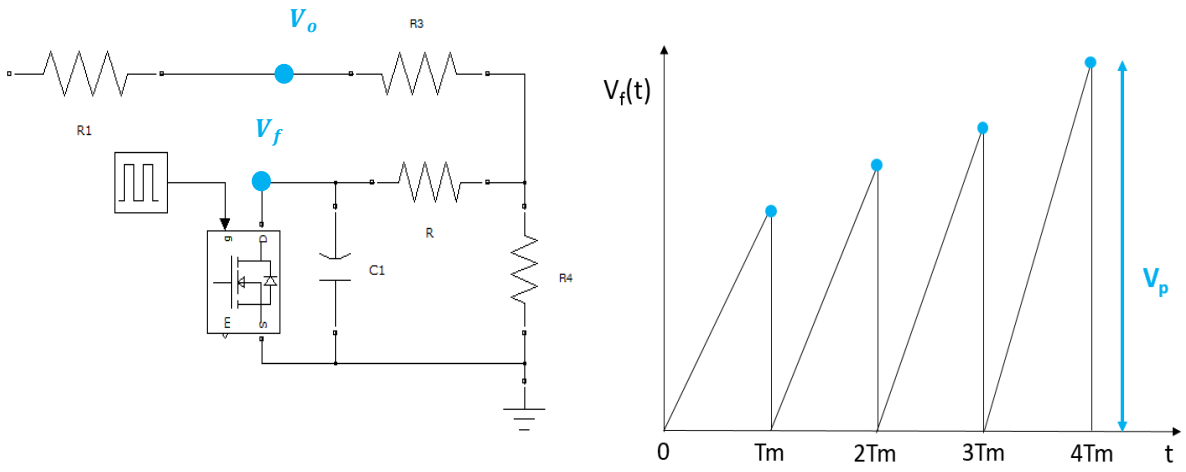

Figure 3-4 (a) Feedback control circuit and generated (b) voltage controlled sawtooth signal

The feedback control circuit is essentially a voltage controlled sawtooth signal generator and is formed by the following components: 4 resistors, 1 capacitor C_1, a MOSFET and a PWM generator. When the MOSFET is switched off, the sawtooth voltage V_f rises, when the switch is on, the voltage V_f reaches its peak value and drop off to zero, V_f can be expressed as follows:

$$V_f(t) = V_0 \frac{R_4}{R_4 + R_3}(1 - e^{-(R+R_3R_4/(R_3+R_4))^{-1}t/C_1}) \tag{3.2}$$

Where V_0 is the voltage of the energy storage element, R_3 and R_4 are the resistor in the feedback circuit, t is the time when the switch is off:

$$t = (1 - D_m) * T_m \tag{3.3}$$

Where D_m is the duty cycle of the PWM generator in the feedback control circuit and T_m is its period.

If $R \gg R_3$, $R \gg R_4$ and the switching period t is far smaller than the time constant in the RC circuit $t \ll RC_1$, the peak voltage of sawtooth V_p can be approximated as a simple expression (3.4) [62]:

$$V_p(t) = V_0 \frac{R_4}{R_3 + R_4}\left(\frac{1 - D_m}{RC_1}\right)T_m \tag{3.4}$$

Once the value of resistors R_3 and R_4, the duty cycle of the PWM generator D_m and its period T_m is set, the peak value $V_s(t)$ is only determined by the voltage of the energy storage element V_o, as is shown in figure 3-4(b). While charging, the voltage output V_o will increase with time, thus the peak value of the sawtooth signal $V_s(t)$ will increase with time. Vise verse, $V_s(t)$ will decrease while energy storage element is discharge.

3.1.3. PWM generate circuit

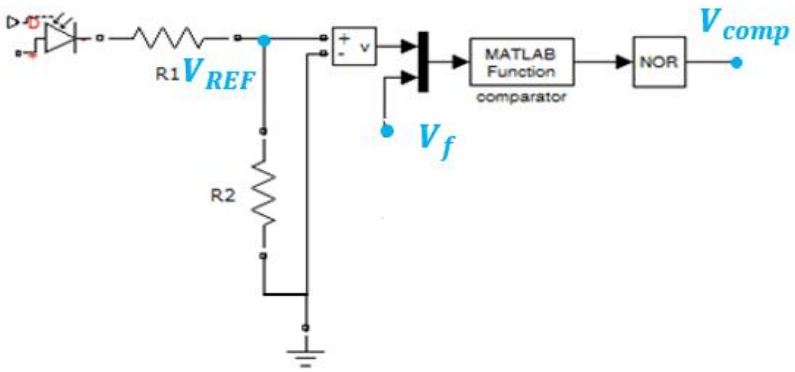

Figure 3-5 PWM generate circuit

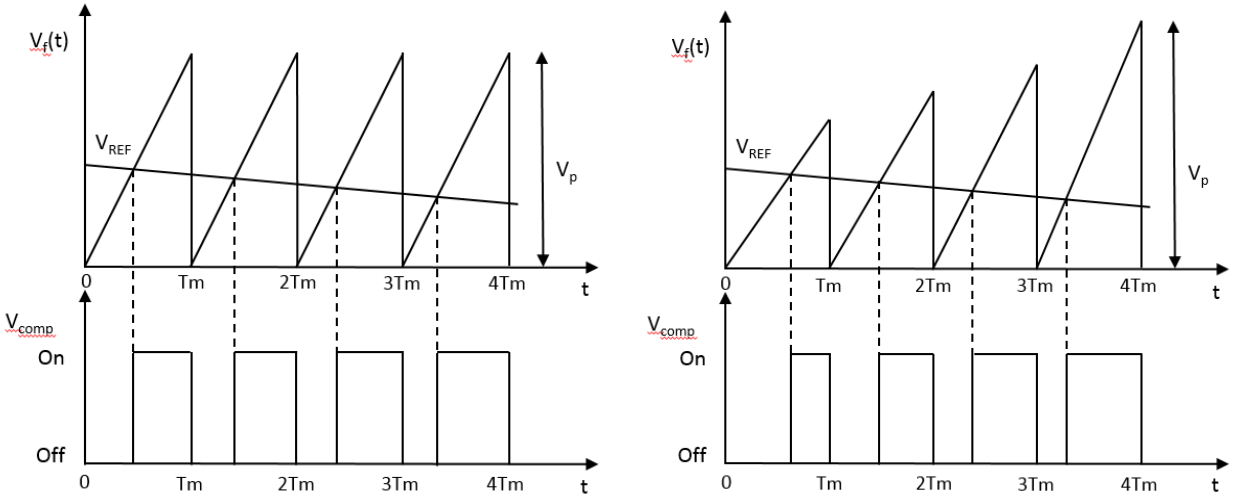

Figure 3-6 Waveforms in comparator (a) with change of ambient light intensity (b) with change of both ambient light intensity and energy storage element condition

The PWM generate circuit is shown in figure 3-5 and is formed by a light sensor, a comparator, a NOT gate and the sawtooth signal source V_f generated in feedback control circuit. The waveform generated in the PWM generate circuit is demonstrated in figure 3-6. By passing through a comparator, the reference voltage V_{REF} from the light senor and the sawtooth signal V_p from the feedback control circuit will be compared and a PWM signal V_{comp} with different duty cycle is been generated. The relationship between peak voltage V_P and reference voltage V_{REF} is:

$$\frac{t'}{T_m(1-D_m)} = \frac{V_P - V_{REF}}{V_P} \tag{3.5}$$

V_{REF} is the voltage division from light sensor which is proportional to light intensity (the voltage output from solar panel V_i is also bind to V_{REF}) , V_p is the peak voltage of sawtooth signal, t' is switch on time of MOSFET in DC-DC converter.

According to the definition,

$$D' = \frac{t'}{T_m} \tag{3.6}$$

Where D' is the duty cycle of the PWM signal generated in the comparator.

As a result of the NOT gate after the comparator, the relationship between the duty cycle of the PWM signal and the duty cycle of the MOSPHET in DC-DC converter is:

$$D = 1 - D' \tag{3.7}$$

Substituting equation (3.5)-(3.7) into (3.4) forms a relationship between output voltage of the proposed and input voltage:

$$\frac{V_o}{V_i} = \frac{\frac{1}{d} + \frac{T_m}{RC_1}}{\frac{T_m}{RC_1}} \tag{3.8}$$

Where T_m is the cycle of the MOSPHET in feedback circuit, and d is sensitivity of light sensor defined as $d = \frac{V_{REF}}{V_i}$, R and C_1 is the resistor and capacitor in feedback control circuit.

As we can see from figure 3-6(a), when voltage output from light sensor V_{REF} is decreasing, which represents the decrease of ambient light intensity, the duty cycle of the PWM signal V_{comp} generated in the comparator is increasing. In figure 3-6(b), when the power storage element voltage increases while charging, the peak voltage of the sawtooth V_p will increase with time, the duty cycle of the PWM generated in the comparator will also change accordingly.

Compared with the feedforward based boost-converter method for MPPT, the implementation of the feedback control gives the ability to maintain MPPT while small fluctuation of voltage in the energy storage interpolates. The duty cycle of the PWM generated in the comparator not only change with ambient light intensity change, but adjust with the energy storage voltage fluctuates. From the final relationship between the output and input voltage, (3.8), we can see that the output voltage remains same once the components in the circuit is set. By testing the solar panel MPP and adjust the circuit, we can autonomously achieve the MPPT algorism.

3.2. Simulation result

In demonstration of the passive MPPT circuit function, the light intensity was set to rise from 150 w/m^2 to 250 w/m^2 within 0.1 second, which is a very large change in light intensity within a short time. The simulation is done in matlab Simulink and the simulation set up is similar as figure 3-2.

Figure 3-7 shows the three voltage signals flow through the feedforward and feedback control of a DC-DC boost converter circuit. The dash dot line is divided voltage from light sensor V_{REF}, the dot line represents the sawtooth voltage V_f generated in feedback control circuit, the solid line is the PWM signal that control the MOSFET in the DC-DC converter. We can see the PWM signal which will control the MOSFET in the boost circuit, is a reverse version of the PWM signal generated in figure 3-6. It is because the signal passed through a NOT gate and the signal get reversed, the duty cycle of this control PWM signal will proportional to the light intensity. In figure 3-7, when V_{REF} increase, the duty cycle in PWM control signal also increases.

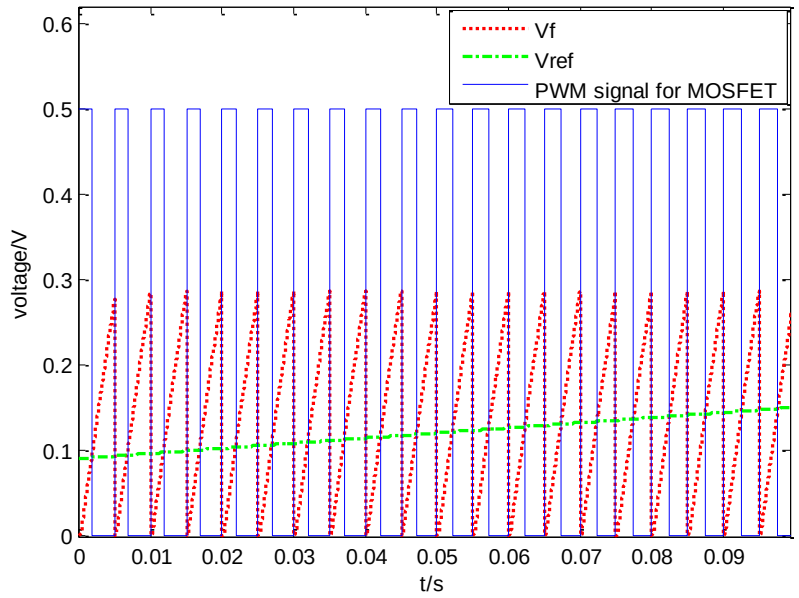

Figure 3-7 Sawtooth voltage Vf, light sensor voltage V_REF and the PWM signal into MOSFET in DC-DC converter

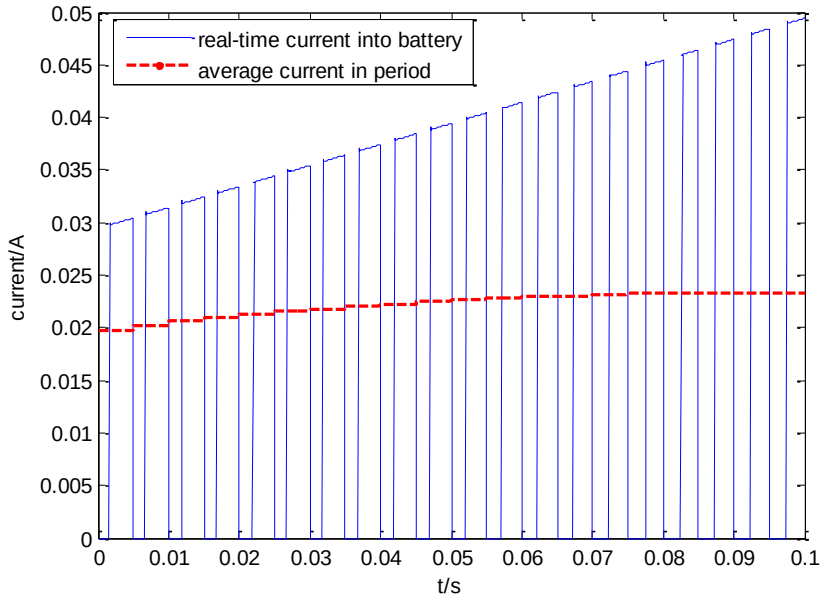

Figure 3-8 Real time charging current into battery v.s. average current

Figure 3-8 shows the real time current flow from DC-DC converter into the energy storage element (solid line) and the mean value of current (dash line) in one period. The current provided by solar panel increases along with the light intensity, but with the implementation of feedforward

and feedback control, the duty cycle of the current is decreased in each period. Thus the mean value of current in each cycle keep stable.

Since the solar panel is a voltage limited current source, when the loading of the circuit remains the same, the voltage of the solar panel will keep in certain range despite the light intensity change in ambient environment. The MPPT task is achieved.

The power generated for small solar energy harvester (total size $0.5 \times 2.5''$) is about 40~50 mW under the light intensity of 200 w/m^2 in average, it is already suitable for long term tracking study use. But for accurate tracking study, frequently GPS data and wireless sensor node included ambient condition data (i.e. temperature, humidity) are needed, thus we need electromagnetic energy harvester to produce more energy.

3.3. Conclusion

In this section, a feedforward and feedback control of a DC-DC boost converter is used for MPPT. The light sensor based feedforward control ensures the MPPT while the ambient light intensity is changing and the feedback control helps dealing with the voltage ripple in the energy storage elements. The systematic analysis and simulation result shows the function of maintain the voltage range of a solar panel with the environmental light intensity change.

4. Broad Bandwidth Pendulum Energy harvester

In this chapter, a novel mechanical motion regulator based electromagnetic pendulum energy harvester (MMR-PEH) is proposed and investigated. Design, modeling, dynamic analysis and experimental verification will be presented in the following sections.

4.1. Introduction of pendulum energy harvester design

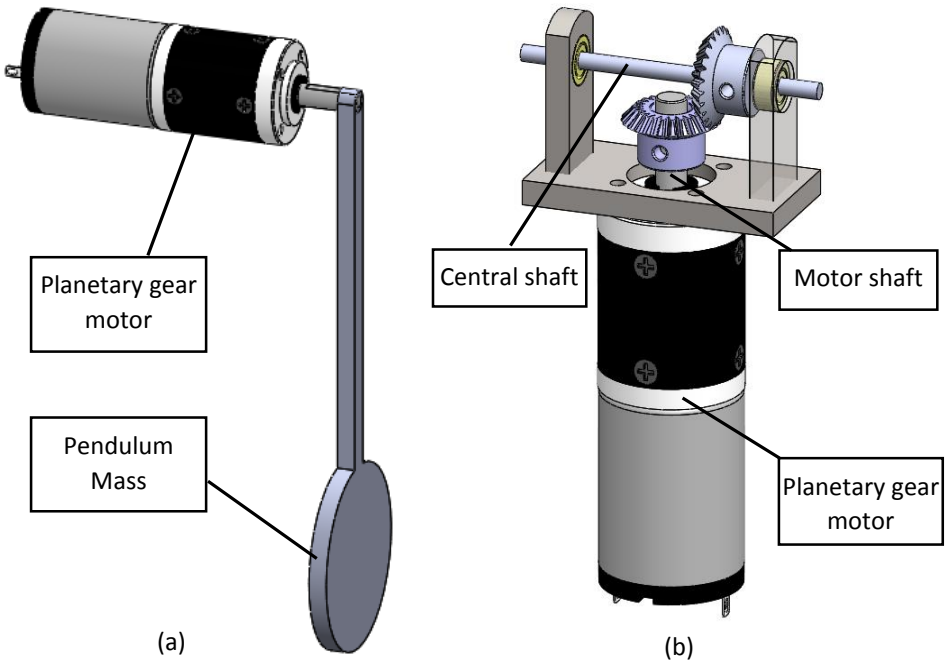

Figure 4-1 (a) Traditional pendulum energy harvester and (b) non-MMR pendulum energy harvester

Figure 4-1 shows two concepts for pendulum based energy harvester design, 4-1 (a) is a traditional pendulum Mass attached to a planetary gear motor, the pendulum mass will wave along the motor shaft and the planetary gear motor can harvest energy from the waving motion of pendulum mass. 4-1 (b) is a non-MMR pendulum energy harvesters, which is formed by a central shaft which is fixed to a base, a planetary gear motor and a transmission consists of two miter gears that can transmit the waving motion of the motor into the rotational motion of the motor shaft. The waving motion will be transferred into the motor rotation motion and the gear box can enlarge the rotational speed of the waving motion and amplify the voltage output of the gear motor.

Compared with the traditional PEH, non-MMR PEH have advantage on using the mass of planetary gear motor to reduce the overall weight of the energy harvester, thus increase the power output to weight ratio of the energy harvester. However, in both designs the irregular bidirectional motion is directly transmitted, so that the motion on the electromagnetic energy harvester is bidirectional, thus the output from the energy harvester is a irregular AC voltage output. In order to store this generated electric energy, a full-wave bridge rectifier circuit is needed to rectify this AC source waveform into a DC output to store it in our energy storage element.

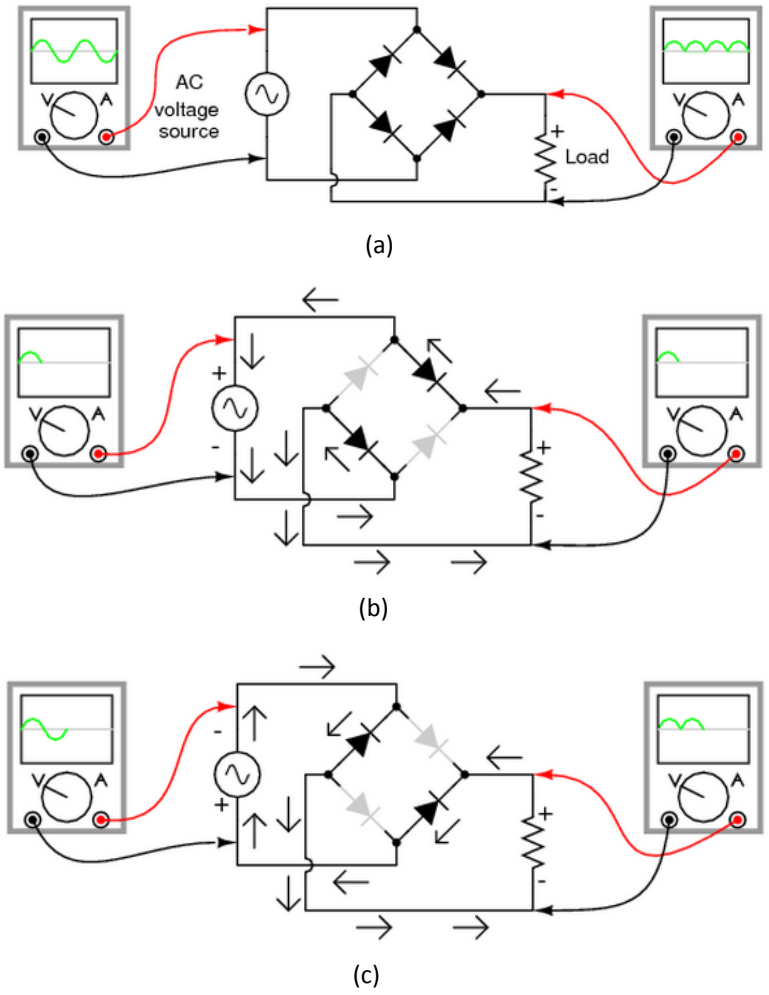

Figure 4-2 (a) Full wave bridge rectifier (b) Electron flow for positive half-cycles and (c) Electron flow for negative half-cycles [63]. Circuits, A.A., Rectifier circuits. http://www.allaboutcircuits.com/vol_3/chpt_3/4.html. Used under fair use, 2015.

Diode allows a one-way flow of electrons in the electric circuit, the principle of diode based full wave bridge rectifier is shown in figure 4-2 [63]. There are four diodes in the circuit, on

positive half-cycles, shown in figure 4-2 (b), the electrons are flowiing through the upright and left bottom diodes. On the negative half cycles, shown in figure 4-2 (c), the electons will pass through the other two diodes. This circuit thus can convert the AC voltage into a DC voltage.

In small silicon diodes, the voltage will drop about 0.6~0.7 volt and in Schottky diodes and germanium diodes, the voltage drop can be around 0.2~0.3 volt as well, making the diode based rectifier circuit the disadvantage of having lower voltage output. The full wave bridge rectifier mentioned above will have two times the voltage drop on a single diode, which is about 0.4~0.6 volt for Schottky diode and 1.4 volt for silicon diode. Since the pendulum energy harvester is normally used in low frequency range range (about 1~10 Hz) and have motion is not large, its voltage output is relativly small. The voltage drop from the rectifier circuit will have a big influence on the energy storage processing. How to reduce or avoide the voltage drop from the rectifier circuit is therefore crucial to improve the energy harvesting efficiency of the pendulum energy harvester.

4.2. Detailed design of broad bandwidth MMR based pendulum energy harvester

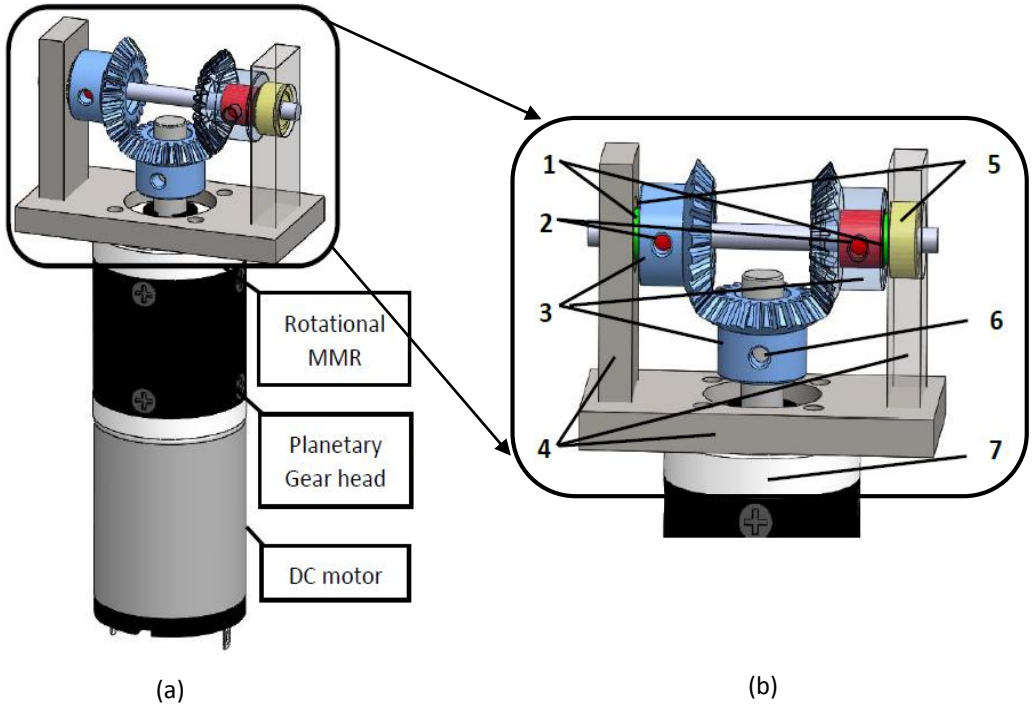

Figure 4-3 (a) detailed design of MMR-PEH and (b) components of the rotational mechanical motion regulator (MMR): 1.Thrust bearing 2. Roller/one way clutch 3. Miter gear 4. Fixture 5. Ball bearing 6. Planetary gearhead shaft 7. Planetary gearhead

As is mentioned in section 4.1, for a design of pendulum energy harvester, the efficiency will be largely increased if we can avoid the rectifier circuit for the energy storage processing. A mechanical motion regulator based design is proposed which can mechanically rectify the bidirectional waving motion of the pendulum into a unidirectional rotational motion on the energy harvester.

Figure 4-2 shows the detailed design of proposed MMR-pendulum energy harvester, it is composed of three parts: a rotational mechanical motion regulator, a planetary gearhead and a DC motor act as a generator. The planetary gearhead is connected between a DC motor and the bottom plate of the rotational MMR and can transmit the lower rotational speed on the gear shaft to a faster rotational speed on the DC motor. The DC motor together with the planetary gearhead is acting as a pendulum and together they will swing along the central shaft which is fixed to a steady base. The rotational MMR is essentially a transmission part between the pendulum and the planetary gearhead shaft, it can transfer the waving motion of the pendulum to the rotational motion of the

gearhead shaft, also will rectify the two directional motion into a unidirectional motion. The structure of rotational MMR is shown in figure 4-2 (b), it is formed by one central shaft, two roller clutches, three miter gears, two ball bearings and some fixtures to hold all the components. In order to explain the mechanism of rotational MMR clear, I would like to introduce the principle of roller clutch or one way clutch.

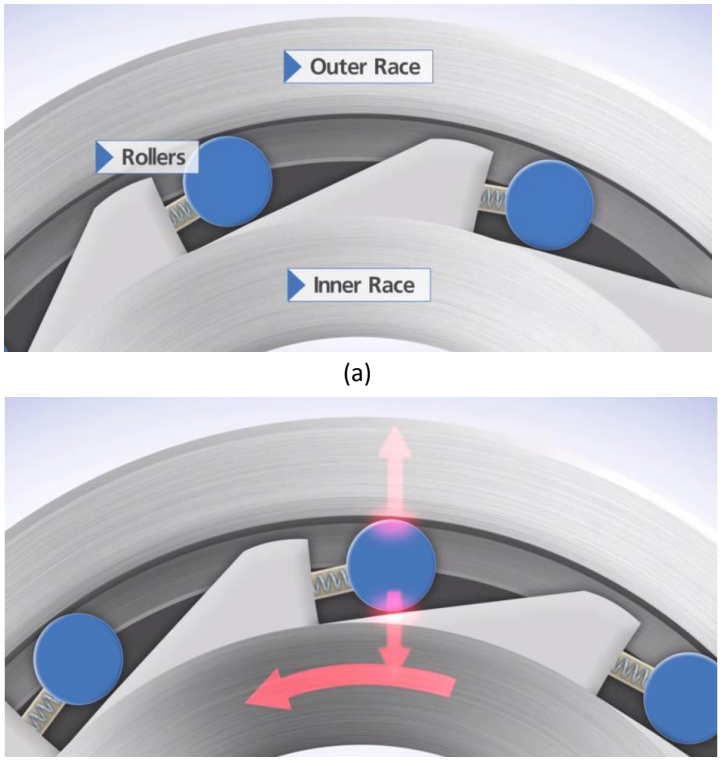

Figure 4-4 (a) internal structure of roller clutch and (b) its working principle [64], RENOLD, Trapped Roller Clutches. http://www.renold.com/Products/TrappedRollerFreewheels/TrappedRollerFreewheels.asp. Used under fair use, 2015.

The internal structure and the working principle of the roller clutch is shown in figure 4-4 [64]. It's formed by a cylindrical outer race, an inner race with ramps and individually sprung rollers. The springs ensure that the rollers are hold in contact with both outer race and inner race ramp and the introduction of ramp on the inner race gives some interesting mechanism for the roller clutch: when the relative motion between the inner race and the outer race is clockwise, the spring is been compressed, the rollers are acting as a planetary gears and rotate freely, we call this disengage period. During this disengage period, roller clutch will act as a regular bearing and there will be no torque transferred between the inner race and outer race. When the relative motion

between the inner race and the outer race is counterclockwise, shown in figure 4-4 (b), the spring will be extended. The ramp on the inner ramp will squeeze the rollers, cause friction between the rollers and the outer ring and transfer torque between the inner race and outer race, this is also known as engage phenomenon. One thing to point out is that during disengage period, the rollers is always contact with the outer race, when the roller clutch change from disengage to engage, the torque transmission will happen instantaneously.

The function of roller clutch is that the torque/motion is only transmitted in one way, videlicet it will have low impediment for torque /motion transmission in one direction and have high resistor on the other. This nonlinearity of motion regulation acts very similar to a diode and essentially the roller clutch can be regarded as a mechanical diode. Unlike electrical diode, this mechanical regulator will not cause torque drop during the transmission, in electrical circuit-voltage drop. Since the rolling friction between the rollers and outer race during disengage period can be almost ignored. In other words, there will very little, if not totally no, energy lose during this mechanical motion rectification. Based on this mechanism of roller clutch and the principle of electrical diode based full wave bridge rectifier, we proposed our design of pendulum energy harvester with rotational mechanical motion regulator (MMR).

The design of proposed rotational MMR is shown in figure 4-3 (b), one central shaft is fixed with a situational base and won't rotate, two miter gears are press fit with two roller clutches. Those two roller clutches are set in the opposite directions, and because of the disengage property of the roller clutch, one of the roller clutches can rotate freely along the central shaft clock wisely while the other one can rotate freely counter clock wisely. Vise verse, on the contrary to the free rotate direction, the roller clutch will engage and transmit torque. Since the roller clutch is connected with the fixed central shaft, during the engage period, it will lock with the shaft, transmit torque from the shaft to the gears connected to the roller clutch, and not moving at all. Two support frames, one bottom plate are holding the weight of the planetary dc motor and connected to the stationary central shaft with regular ball bearings, they will wave together along with the shaft as a pendulum. Two miter gears are press fit with two roller clutches and will rotate together with them. When the roller clutch is engaged, the miter gear connected to it will be locked on the stationary central shaft and in turns transfer torque to the third miter gear connected with the planetary gearhead shaft. The two miters are set in different directions to the third miter gear and

they are engaging and transferring torque miter at different waving period, making the third miter gear, or the input of planetary dc motor, rotating in the same direction.

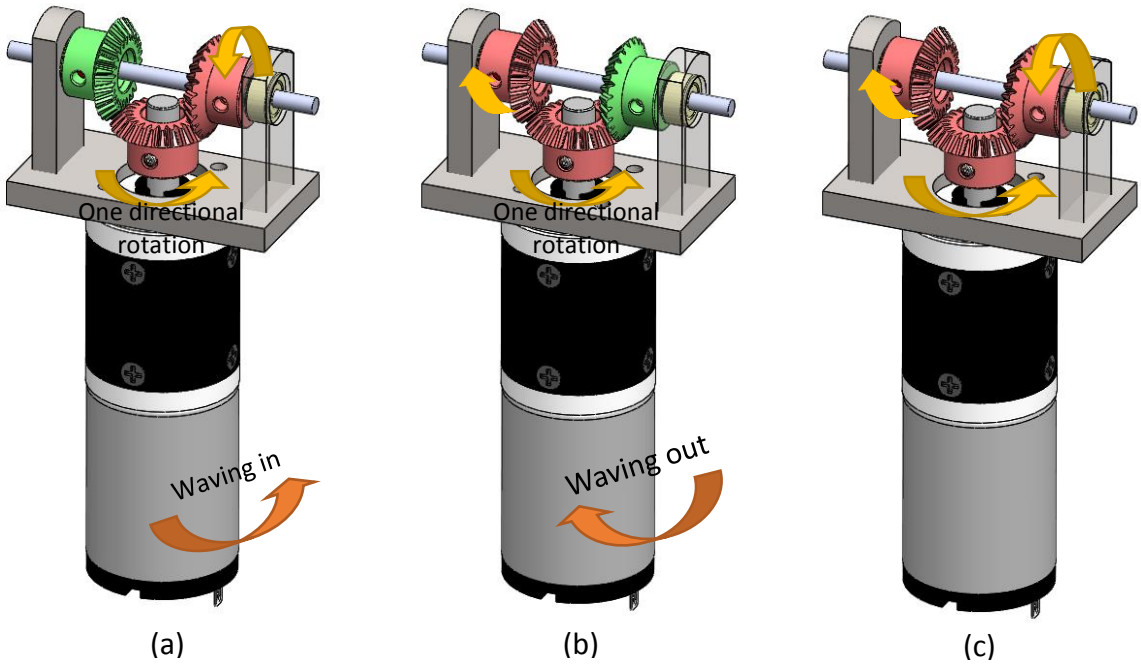

Figure 4-5 working principle of rotational MMR at different waving period: (a) waving in (b) waving out and (c) the planetary gearhead shaft disengaged from the rotational MMR

Figure 4-5 shows the working principle of rotational MMR based pendulum energy harvester at different waving periods. When the pendulum mass/ geared motor is waving in, figure 4-5 (a), the left roller clutch will engage (marked as green) and the right one will disengage (marked as red) from the central shaft. The miter gear on the left will lock with the shaft and stop the left teeth of the bottom gear from going in along the shaft, this will drive the bottom gear to rotate counter clockwise. When the pendulum mass is waving out plane, shown in figure 4-5 (b), the right roller clutch will engage and the left one will disengage, stop the right teeth of the bottom miter gear from coming out plane along the shaft. This will also force the bottom gear to rotate counter clockwise. In summary, in utilizing the nonlinearity (engage/disengage property) of a roller clutch, the rotational MMR can convert the irregular bidirectional waving motion of the pendulum into a unidirectional rotational motion on the electromagnetic energy harvester, hence the voltage output from the electromagnetic energy harvester is a DC output. Compared with the pendulum energy harvester designs in figure 4-1, rotational MMR based pendulum energy harvester can rectify the bidirectional waving motion of the pendulum into a unidirectional

rotational motion mechanically. So we can prevent from using electrical diode based full wave bridge rectifier for energy storage circuit, avoid the voltage drop on diode and increase the efficiency of harvesting energy from mechanical motion.

One interesting phenomenon in the rotational MMR is that, when the absolute (ignore the direction of in or out plane) waving motion on the planetary gearhead shaft is larger than the waving motion of the pendulum, both left and right miter gears will disengage from the shaft, shown in figure 4-5 (c). When this total disengage happens, there will be no contact force/torque between the fixed shaft and the planetary gearhead shaft, the gear shaft will then rotate freely with an initial rotational speed (which is the speed when the total disengage just happened). Since the gear shaft is connected to a dc motor, the electrical damping (if the motor is in close loop) and the rotational inertia of the dc motor will have influence on the motion of the gear shaft. The gear shaft will reduce the initial speed by the effect of damping in a certain ratio, once this rotational speed is caught up by the waving speed of the pendulum, the bottom gear will engage again with the fixed shaft. This total disengage mechanism of the rotational MMR gives this system a very important property: the planetary gearhead shaft is always tend to rotate in a higher rotational speed when the pendulum waving cannot provide enough motion for it. For traditional rigid motion transmission system like rack pinion system and gear transmission system, the rotational speed of a driven system cannot exceed the speed of driving system. Our proposed rotational MMR, however, is act differently. When the pendulum waving motion can provide enough power, the rotational MMR will transfer torque and drive the gearhead shaft to rotate in the same speed of pendulum. However, when the pendulum waving motion is slower than the gearhead shaft rotational motion, the gearhead shaft will disengage from the rotational MMR, rotate on a higher but decaying speed until the waving speed is become larger. This nonlinearity of total disengage of the rotational MMR will help increase the power output of the energy harvester and the pendulum system will have a broader bandwidth frequency response compared with traditional rigid connected single DOF system. We will show these properties in the next sections.

4.3. Modeling and analysis of prototype

The design and working principle of rotational MMR based pendulum energy harvester is explained in section 4.2. The motion of the MMR-PEH can be split into two periods: engage period

and total disengage period. When the waving speed of pendulum is equal or greater than the rotational speed of the gearhead, the dc motor based energy harvesting system get engaged and the pendulum system will drive the energy harvesting system and move together. In this period, the electrical damping and rotational inertia in the energy harvesting system will influence the motion of pendulum system. When the waving speed of pendulum starts decreasing and the rate of decreasing (or acceleration) is larger than the decreasing on the gearhead, the energy harvesting system will be totally disengaged. In this period, the single DOF pendulum system in the engage period will be switched into a two DOF system – geared motor system decaying with initial speed and a pendulum system. The energy harvesting system starts with an initial rotational speed and the speed decays due to the electrical damping provided in the dc motor circuit. The pendulum system, during the total disengage period, will keep its own waving motion. The electrical damping and rotational inertia will not have contribution for the motion of pendulum during this period.

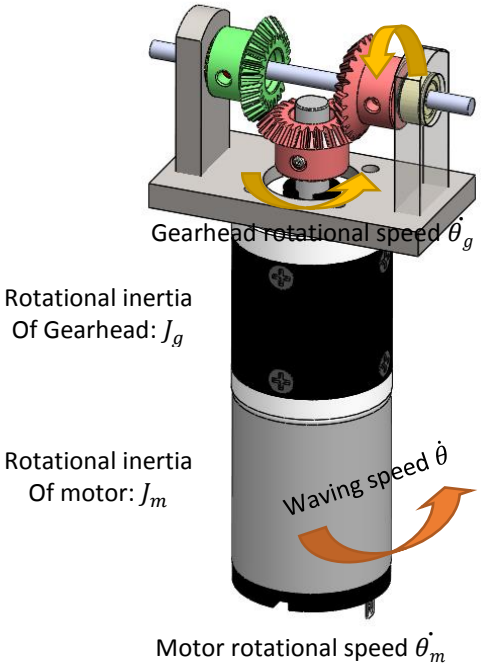

Figure 4-6 nomenclature of rotational MMR pendulum energy harvester

The nomenclature for the rotational MMR pendulum energy harvester is shown in figure 4-6. The rotational inertia of the pendulum mass along the shaft is J_θ, the rotational inertia of gearhead is J_g and the rotational inertia of motor is defined as J_m. The angular waving speed of pendulum is $\dot{\theta}$, the angular rotational speed on the gearhead is $\dot{\theta_g}$ and the rotational speed on the

motor shaft is $\dot{\theta_m}$. When the system is engaged, the relationship between this different speed are shown in (4.1):

$$\dot{\theta} = \frac{\dot{\theta}_g}{R_b} = \frac{\dot{\theta}_m}{R_b R_g} \tag{4.1}$$

Where R_b is the gear ratio of bevel gears, if we are using the miter as transmission, the ratio would be 1. R_g is the gear ratio of the gearbox.

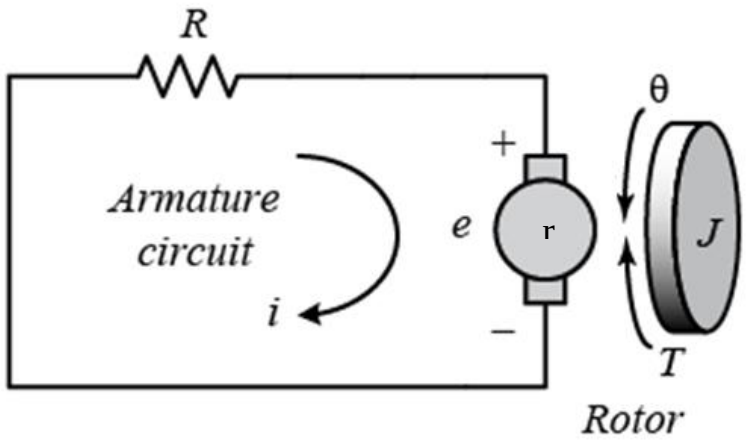

Figure 4-7 the electric circuit of the armature and the free-body diagram of the rotor [65]

In the MMR-PEH design we are using a brushed dc motor as an energy harvester, when the dc motor is rotating, it can generate voltage in the circuit. Also the current conducted by the generated voltage will in return give torque on the rotor. This processing can be explained in figure 4-6.

The generated voltage is proportional to the rotational speed of the rotor and their relationship is:

$$e = K_e \dot{\theta}_m \tag{4.2}$$

Where K_e is generator constant of the dc motor.

The motor has its own internal resistor r and if the motor is simply connected to an external resistor R, the current generated in the circuit is:

$$i = \frac{e}{R+r} \tag{4.3}$$

The power can be generated on the external resistor is:

$$P = \frac{e^2 R}{(R+r)^2} \tag{4.4}$$

To the gearhead shaft, the current induced torque is:

$$\tau = R_g R_b K_t i \tag{4.5}$$

Where K_t is torque constant of the motor, R_b and R_g are gear ration on bevel gear and gearhead.

Subscribe equation (4.2) and (4.3) into (4.5), we can get the relationship between the rotational speed of the motor and the corresponding feedback torque from the electric circuit:

$$\tau = \frac{K_e K_t R_g R_b \dot{\theta}_m}{R+r} \tag{4.6}$$

Using the Euler-Lagrange equation, we can get the equation of motion of the MMR-PEH system. The kinetic energy in the MMR-PEH system is:

$$T = \frac{1}{2} J_\theta \dot{\theta}^2 + \frac{1}{2} J_g \dot{\theta}_g^{\,2} + \frac{1}{2} J_m \dot{\theta}_m^{\,2} \tag{4.7}$$

The potential energy in the MMR-PEH system is:

$$V = -MgL(1-\cos\theta) \tag{4.8}$$

Where M is the overall mass of the PEH is, L is the length between the central shaft and the center of mass of the PEH, θ is the angle between the current position to the equilibrium position.

$$L = T - V \tag{4.9}$$

Assume the external force is applied to the pendulum central shaft and there is a small angle shift in the system $\delta\theta$, the virtual work can be represented as:

$$\delta W = FL\delta_\theta - \tau\delta_\theta \tag{4.10}$$

Subscribe equation (4.6) into (4.10):

$$\delta W = (FL - \frac{K_e K_t \dot{\theta}_m}{R+r} - c_m\dot{\theta}_m)\delta_\theta \tag{4.11}$$

c_m is the mechanical damping in the pendulum system.

Generalized force is thus:

$$Q_i = FL - \frac{K_e K_t \dot{\theta}_m}{R+r} - c_m\dot{\theta}_m \tag{4.12}$$

The Euler-Lagrange equation:

$$\frac{d}{dt}(\frac{\partial L}{\partial \dot{Q}_i}) - \frac{\partial L}{\partial \dot{Q}_i} = Q_i \tag{4.13}$$

Subscribe (4.1)~(4.12) into (4.13), we can get the equation of motion of the system during engagement:

$$(J_\theta + J_g R_b^2 + J_m (R_g R_b)^2)\ddot{\theta} + (\frac{(R_g R_b)^2 K_e K_t}{R+r} + c_m)\dot{\theta} + MgL\sin\theta = FL \tag{4.14}$$

Define that:

$$m_s = J_g R_b^2 + J_m (R_g R_b)^2 \tag{4.15}$$

$$c_e = \frac{(R_g R_b)^2 K_e K_t}{R+r} \tag{4.16}$$

Where m_s is the rotational mass of dc motor added to the pendulum when the system get engaged and c_e is the electric damping from the dc motor, c_m is the damping to the waving velocity, the corresponding damping force is $F = \dot{\theta} c_m$. When the waving speed of the pendulum is larger than the rotational speed of the gearhead shaft, system get engaged, the equation of motion for the MMR-PEH (4.14) can be rewrite as:

$$(J_\theta + m_s)\ddot{\theta} + (c_e + c_m)\dot{\theta} + MgL\sin\theta = FL \tag{4.17}$$

This is essentially an equation of motion of a pendulum system. When the waving speed of pendulum $\dot{\theta}$ is smaller than the rotational speed on the planetary gearhead shaft $\dot{\theta}_g$, total disengage will happen, the system will be separated into a two DOF system, a simple pendulum system:

$$J_\theta \ddot{\theta} + c_m \dot{\theta} + MgL\sin\theta = FL \tag{4.18}$$

And a close loop motor system with initial speed:

$$m_s \ddot{\theta}_m + c_e \dot{\theta}_m = 0 \tag{4.19}$$

And as is mentioned m_s and c_e are corresponding motor inertia and its electrical damping.

Sum equation (4.17)~(4.19), we can get the dynamic equation of the overall MMR-PEH, it's essentially a switched linear system:

$$\begin{aligned} &\text{engage: } (J_\theta + m_s)\ddot{\theta} + (c_e + c_m)\dot{\theta} + MgL\sin\theta = FL \\ &\text{disengage: } \begin{cases} J_\theta \ddot{\theta} + c_m \dot{\theta} + MgL\sin\theta = FL \\ m_s \ddot{\theta}_m + c_e \dot{\theta}_m = 0 \end{cases} \end{aligned} \tag{4.20}$$

As was mentioned, the switch criteria of the MMR-PEH between engage and total disengage is:

$$\begin{cases} \dot{\theta} \geq \dot{\theta}_g \ \ system\ disengage \rightarrow engage \\ \ddot{\theta} < \ddot{\theta}_g \ \ system\ engage \rightarrow disengage \end{cases} \tag{4.21}$$

Where $\dot{\theta}_g$ and $\ddot{\theta}_g$ are angular speed and angular acceleration on the gearhead shaft, the relationship between $\dot{\theta}_g$ and $\dot{\theta}$ is shown in (4.1). This processing can be visualized as figure 4-8.

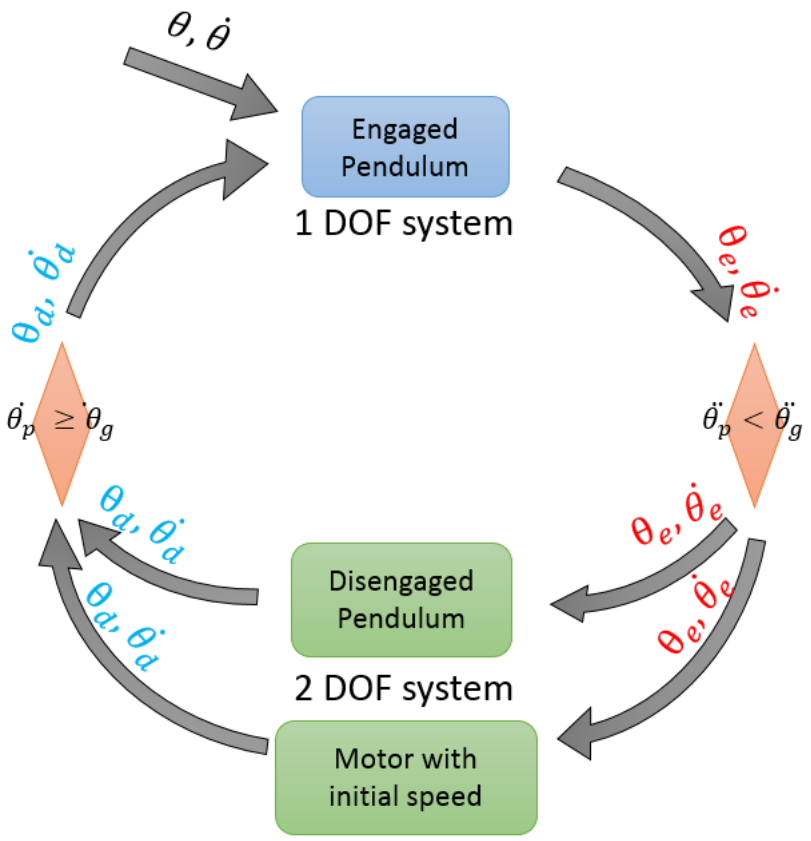

Figure 4-8 the switching loop of the MMR-PEH system

The MMR-PEH system starts with some initial θ and $\dot{\theta}$, since the motor system have no rotational speed, it will engage with the pendulum system, the pendulum will drive the motor and they will move together following the dynamic equation (4.17). When the speed of engaged pendulum starts to decrease and the state variables match the switching condition $\ddot{\theta}_p < \ddot{\theta}_m$, the single DOF system will immediately switch into a two DOF system: a disengaged pendulum system and a motor with initial speed.

One thing needed to be point out is that the state variables of system, i.e. θ_e and $\dot{\theta_e}$, will remain the same at the instance right before and after the switch, the passed status from engage to disengage is marked as red in figure 4-8. This instant status pass is due to the structure of roller clutch (mentioned in section 4.1), it can maintain instantaneous torque transmission when switching from disengage to engage. Hence the disengaged pendulum will start the motion described in (4.18) with some initial status θ_e and $\dot{\theta_e}$ and the motor system will also have some initial speed $\dot{\theta_e}$ and start decaying this speed following the dynamic equation described in (4.19).

These two systems keep going independently, following their owe dynamics, until the state variables match the switch condition from disengage to engage. These two independent systems will switch back again to a single DOF system and start the switching loop again. As was happened during the switching from engage to total disengage, the angular speed and acceleration of the engaged system θ_d and $\dot{\theta_d}$, will be exactly the same as those before the switch. For this switched system, it is an energy dissipative linear system during each switching period, the initial condition in the start will be dissipated after several cycle. However, the variable status passed between the switch will always be there. The simulation result for this nonlinearity of this switched linear system will be talked about in the next section.

4.4. Dynamic analysis of pendulum energy harvester with MMR – case study on a MMR-PEH prototype

In this section, a linearized model of a MMR-PEH prototype is analyzed as a case study, properties like time domain signal, phase portrait, frequency response are shown. Influence of designable parameters like external resistor and rotational inertia are studied and optimized. Based the results from the case study, a more general linearized dimensionless model is examined to guide the design of general MMR-pendulum energy harvester.

(a) (b)

Figure 4-9 prototype of MMR-PEH

Figure 4-9 shows a prototype of designed MMR-PEH, we used a 9W maxon motor RE-max-29 and a 14:1 gear ratio gearhead GP-32-A as generator for the MMR-PEH and three 1:1 miter as transmission gears, figure 4-9 (b). The parameters of the MMR-PEH are shown in table 4-1.

Table 4-1 parameters and descriptions of the MMR-PEH

Symbol	Description	Value
M	Mass of overall system	0.45 kg
L	Length between shaft and center of mass	0.05 m
R_b	Gear ratio of the bevel gear	1
R_g	Gear ratio of gearhead	14
c_m	Mechanical damping in the pendulum system	0.002 Ns/m
J_θ	Rotational inertia of pendulum	1.4868 gm^2
J_m	Rotational inertia of rotor	13 gcm^2
J_g	Rotational inertia of gearbox	0.8 gcm^2
K_e	motor voltage constant	180 $rpm/volt$
K_t	Motor torque constant	53 mNm/A
r	Internal resistor of the motor	9.24 Ω
R	External resistor	200 Ω

Subscribe the parameters into equation (4.15) and (4.16), we can calculate the added mass into the pendulum system during engagement:

$$m_s = J_g R_b^2 + J_m (R_g R_b)^2 = 2.5488 \times 10^{-4}\ kgm^2 \tag{4.22}$$

The ratio of the added mass over the original rotational inertia of the pendulum can be calculated as:

$$u = \frac{m_s}{J_\theta} = 17.143\% \tag{4.23}$$

The electrical damping of the motor is:

$$c_e = \frac{(R_g R_b)^2 K_e K_t}{R + r} = 2.63382 \times 10^{-3}\ N \cdot s / m \tag{4.24}$$

If the pendulum energy harvester is waving within a small angle, the pendulum motion can be simplified as a linearized mass-spring-damping system for simplification and assume the driving force is a sinusoid force with frequency ω:

$$\begin{aligned} &\text{engage: } (J_\theta + m_s)\ddot{\theta} + (c_e + c_m)\dot{\theta} + MgL\theta = F\cos(\omega t)L \\ &\text{disengage: } \begin{cases} J_\theta \ddot{\theta} + c_m \dot{\theta} + MgL\theta = F\cos(\omega t)L \\ m_s \ddot{\theta}_m + c_e \dot{\theta}_m = 0 \end{cases} \end{aligned} \tag{4.25}$$

And the switching criteria is still:

$$\begin{cases} \dot{\theta} \geq \dot{\theta}_g\ \ system\ disengage \rightarrow engage \\ \ddot{\theta} < \ddot{\theta}_g\ \ system\ engage \rightarrow disengage \end{cases} \tag{4.26}$$

The mechanical and electrical damping ratio of the engaged system can be calculated as:

$$\xi_m = \frac{c_m}{2\sqrt{MgL(J_\theta + m_s)}} = 5.103\% \tag{4.27}$$

$$\xi_e = \frac{c_e}{2\sqrt{MgL(J_\theta + m_s)}} = 6.720\% \tag{4.28}$$

Also the engage and disengage of the added mass m_s will cause the change of nature frequency in the system, the natural frequencies during engagement and disengagement are:

$$f_{engage} = \frac{1}{2\pi\sqrt{MgL(J_\theta + m_s)}} = 1.7907Hz \tag{4.29}$$

$$f_{disengage} = \frac{1}{2\pi\sqrt{MgLJ_\theta}} = 1.9382Hz \tag{4.30}$$

Assume the driving force F a sinusoids input with constant acceleration:

$$F = Ma\sin(2\pi ft) \tag{4.31}$$

Where a is the constant driving acceleration and f is the driving frequency.

A Runge-Kutta RK4 method is employed to solve the dynamical equation of the system (4.25) with switch criteria (4.26) numerically.

Take the waving speed of the pendulum θ as input velocity of the MMR-PEH transmission and the rotational speed of gearhead $\dot{\theta}_g$ as output velocity of the MMR-PEH transmission.

In the first simulation we used a 0.5g acceleration, 3Hz frequency sinusoid driving force to drive this system, the initial position was set to be $(\theta, \dot{\theta}) = (0.2, 0)$. The simulation result of the input and output speed of the MMR-PEH is shown in figure 4-10 and 4-11.

As was mentioned in previous section, the pendulum is waving in two directions around its equilibrium position and because of the nonlinearity of roller clutch, the actual input to the gearhead shaft is a unidirectional absolute waving speed of the pendulum. Figure 4-10 shows the time domain signal of the input and output speed of MMR-PEH transmission under frequency f=3Hz and acceleration a=0.5g. The blue dash-dot line is the pendulum waving speed, it's a bidirectional sinusoid signal. The black dash line represents the actually output of MMR-PEH transmission to the gearhead shaft, it is a unidirectional signal. The red solid line is actual rotational speed on the gearhead.

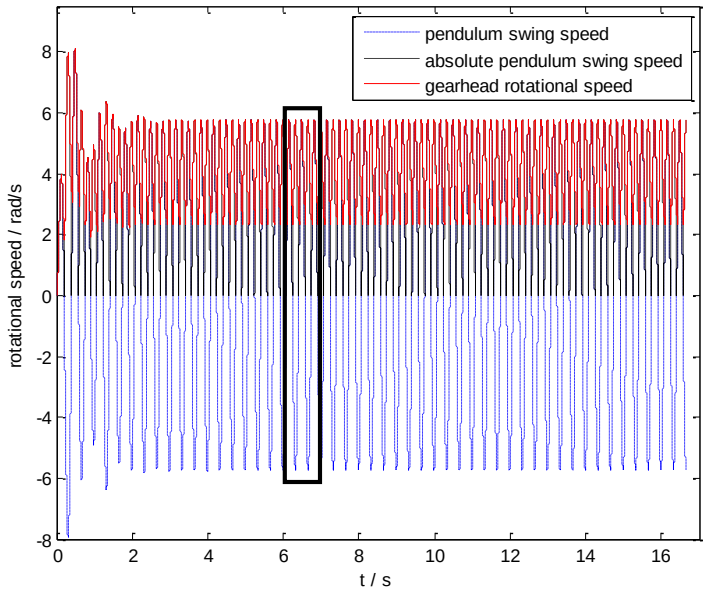

Figure 4-10 Time domain signal of the input and output speed of MMR-PEH transmission, under frequency f=3Hz and acceleration a=0.5g

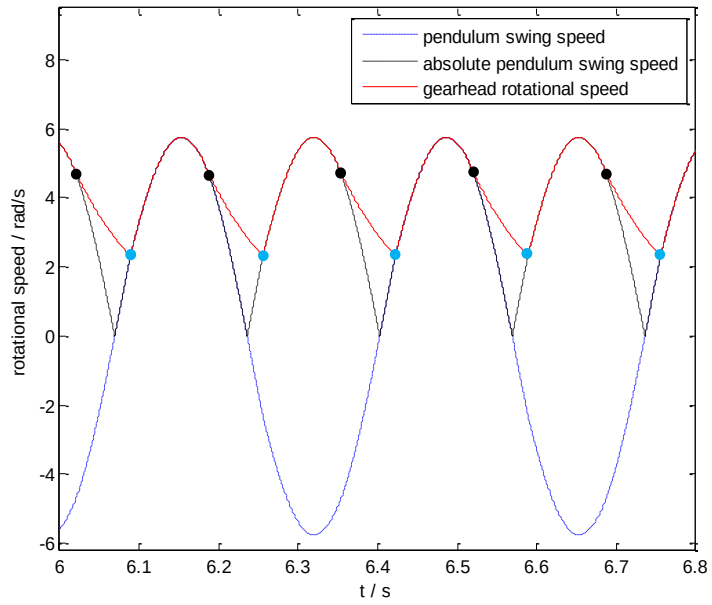

Figure 4-11 Zoomed in signal of time domain input/output speed of MMR-PEH transmission, under frequency f=3Hz and acceleration a=0.5g

Figure 4-11 is zoomed in version of the black block in figure 4-10. The gearhead rotate at the same speed as pendulum waving speed till reached the black dot, where the system parameters

match with the switching condition from engage to disengage: $\ddot{\theta} < \ddot{\theta}_g$. After that the system separates into two systems: the gearhead rotate with an initial speed θ_0 and decay due to its own electrical damping and the pendulum keep waving at its sinusoid speed. These two systems keep on going independently until the pendulum speed $\dot{\theta}$ start increasing and catch up with the decaying speed of the gearhead $\dot{\theta}_g$ at the blue dot in figure 4-11, the MMR-PEH system starts engage and becomes a single DOF system again.

During the total disengage time between the black dot and blue dot, the RMS value of gearhead rotational speed $\dot{\theta}_g$ is always greater than the RMS value of pendulum waving speed $\dot{\theta}$. Therefore, the overall RMS value of gearhead rotational speed is larger than that of pendulum waving speed. From the energy harvesting point of view, larger RMS rotational speed on the DC motor means higher power is harvested. We can draw the conclusion that under 3Hz sinusoid driving force, compared with rigid connected single DOF pendulum energy harvester, the MMR-pendulum energy harvester can harvest more energy from same driving source.

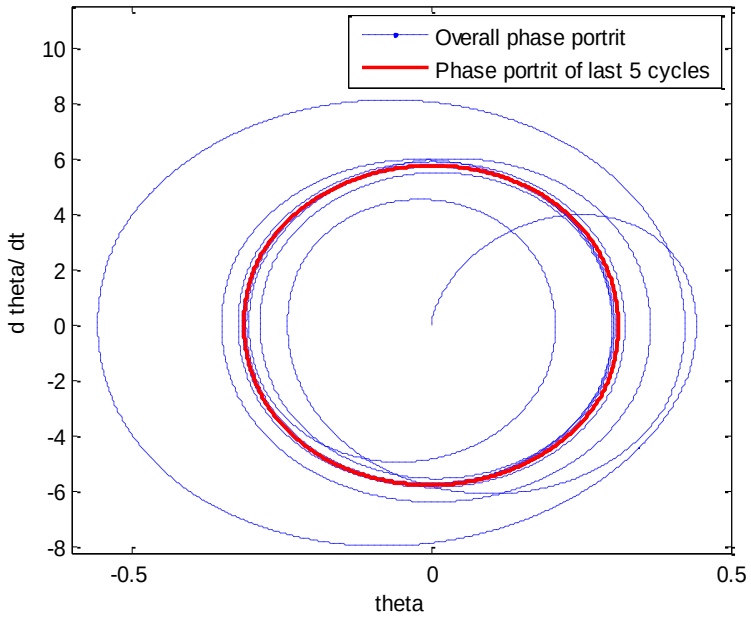

Figure 4-12 Phase portrait of the pendulum motion under 3Hz, 0.5g excitation

Figure 4-12 shows the phase portrait of the overall motion of pendulum within 10 seconds and the phase portrait of last 5 cycles. The pendulum system starts with the initial position $(\theta, \dot{\theta}) = (0, 0)$, after several cycles it settles down to the red ellipsoid curves. The MMR-PEH

system is a switched linear system, it ensures the system the nonlinear property in during its motion. However the phase plot shows that the rotational motion of the pendulum is stable.

In comparison with the performance of MMR-PEH, a pendulum energy harvester with no MMR design is introduced. This non-MMR-PEH has the motor mass and electric damping always connected to the pendulum system and the equation of motion for this non-MMR-PEH can be expressed as:

$$(J_\theta + m_s)\ddot{\theta} + (c_e + c_m)\dot{\theta} + MgL\theta = FL\cos(\omega t) \tag{4.32}$$

It's a pendulum system with added motor mass m_s and electric damping c_e. The close form solution of the time domain averaged power harvested by c_e vs driving frequency ω is [66]:

$$P_{non-MMR-PEH} = \frac{1}{2} c_e \omega^2 \frac{F^2}{[MgL - \omega^2 (J_\theta + m_s)] + \omega^2 (c_e + c_m)^2} \tag{4.33}$$

The MMR-PEH system is a switched linear system and we calculate its power output vs. frequency by integrating the stabilized time domain signal numerically.

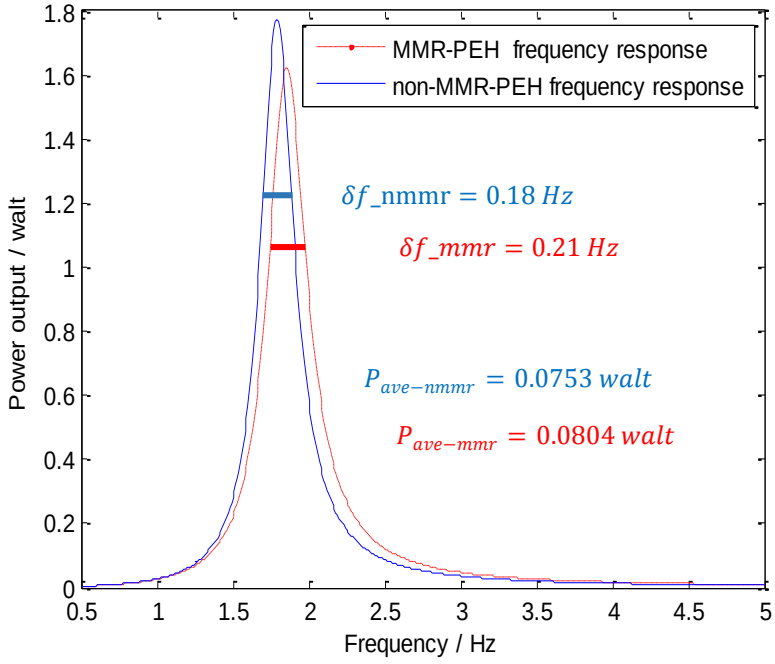

Figure 4-13 Frequency response of the MMR-PEH system and the always engaged non-MMR-PEH

Figure 4-13 shows the frequency response of the MMR-PEH and the always engaged non-MMR-PEH, X-axial is the frequency of the driving force, Y-axial is the average power output from the DC motor during stable period (last five cycles). Both of the systems have same parameters under same driving condition, the only difference is MMR-PEH system can have total disengage of the electrical damping and added mass, non-MMR-PEH the electrical damping and added mass are always engaged. Compared the frequency response of these two systems we can find that the non-MMR-PEH have higher peak at the resonant frequency than the MMR-PEH.

By integrating the frequency response of both systems, the average power density of MMR-PEH over frequency 0.01~6Hz is 0.0804 Walt and the average power density of non-MMR-PEH is 0.0753 Walt. The average power density over frequency represents the power output of the energy harvester driven under white noise, the higher the number the more power could be harvested. We can also draw a horizontal line in the frequency response to determine the bandwidth of the frequency, the height of the line is $\frac{\text{Peak value}}{\sqrt{2}}$. The cross frequency in MMR-PEH covered 0.21 Hz while non-MMR-PEH covered 0.19 Hz, it shows that the MMR-PEH have a broader bandwidth frequency response than the non-MMR-PEH.

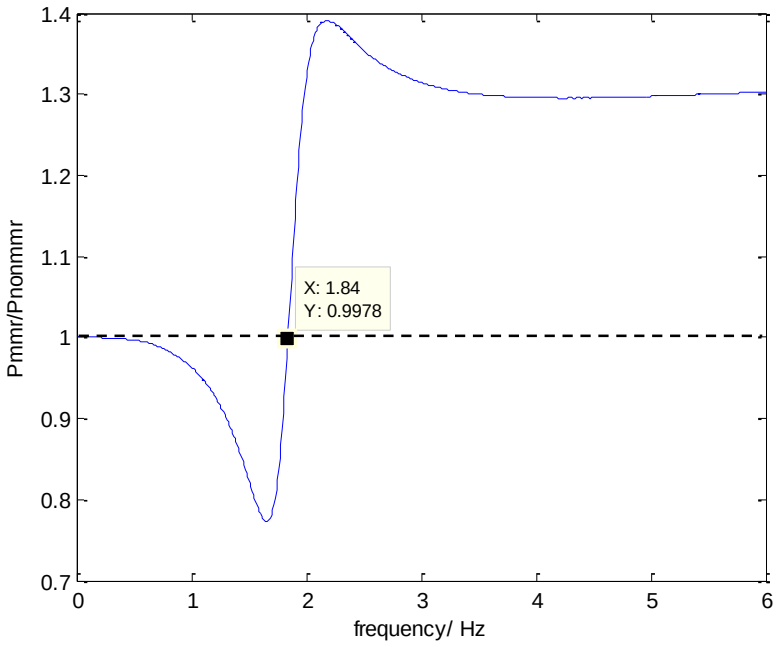

Figure 4-14 power output ratio of the MMR-PEH over non-MMR-PEH vs driving frequency

Figure 4-14 shows the ratio between the power output from MMR-PEH and the power output from non-MMR-PEH vs frequency. The ratio of "1" means under that driving frequency, the power output from MMR-PEH is the same as non-MMR-PEH. When the ratio is larger than "1", the output power from MMR-PEH is greater than non-MMR-PEH. Combine figure 4-14 with figure 4-13, when the driving frequency is smaller than 1.84Hz, the power output from non-MMR-PEH is greater than the power output from MMR-PEH. However when the frequency cross that frequency, the MMR-PEH will always have advantage over non-MMR-PEH.

4.5. Influence of designable parameters

For an already build prototype, we can still change the performance of the MMR-PEH by changing two parameters: the external resistor and rotational inertia.

4.5.1. External resistor

The external resistor can affect the electrical damping of the system, and they have negative correlation, shown in equation (4.16):

$$c_e = \frac{(R_g R_b)^2 K_e K_t}{R + r}$$

The external resistor can also affect the percentage of the power being extracted from the electrical circuit, as was explained in equation (4.4):

$$P = \frac{e^2 R}{(R + r)^2}$$

When the external resistor is very small, the electrical damping added to the system during engage will be very large. This damping will constrain the motion of pendulum waving and greatly reduced the rotational speed on the generator. Though the percentage of power extracted from the electric circuit is increased, but the overall power is reduced, therefore we can't use too small external resistor. If the external resistor is very large, the rotational speed on the generator is enlarged however in the electrical circuit, the power stored on the external resistor is decreased. We need an appropriate external resistor to maximize the power output on the energy harvester.

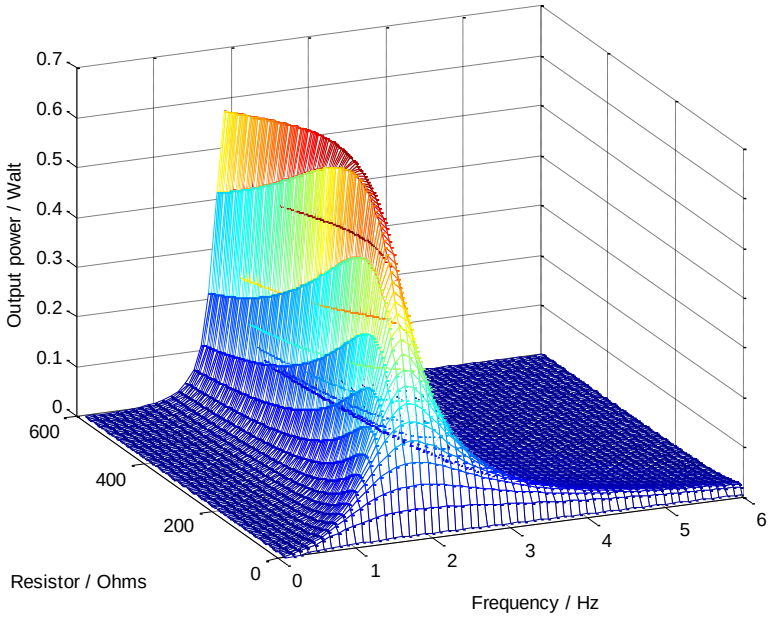

Figure 4-15 mesh plot of external resistor and driving frequency vs output power of MMR-PEH, driven under 0.5g acceleration

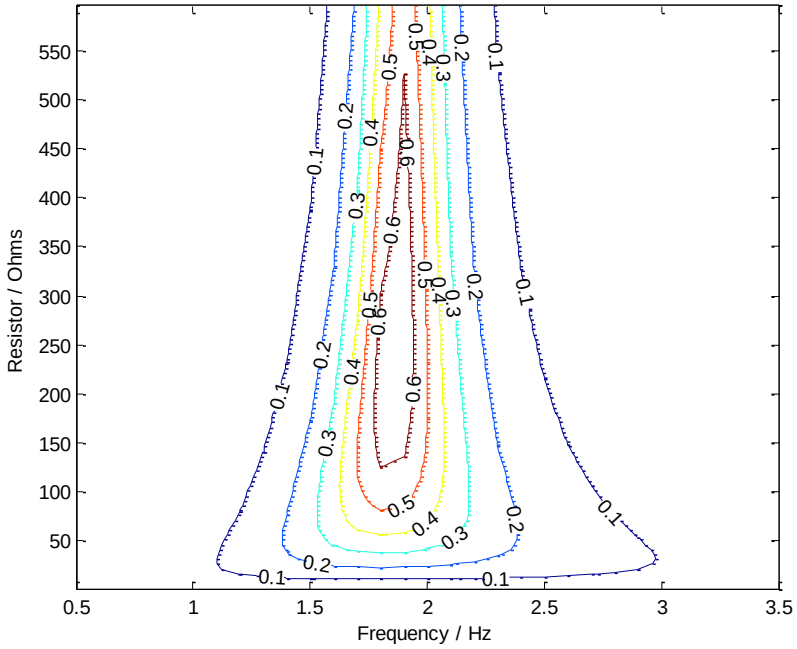

Figure 4-16 contour plot of external resistor and driving frequency vs output power of MMR-PEH, driven under 0.5g acceleration

Figure 4-15 shows the mesh plot and 4-16 shows contour plot of output power on the external resistor vs. the driving frequency and external resistor. It is observed from figure that the output power on the external resistor is highly dependent on the driving frequency. When the driving frequency is close to its natural frequency, around 1.9 Hz, there will be a peak on the 3D mesh plot. When the system is driving at natural frequency, the optimized external resistor is very large since the peak motion is very sensitive to damping in the system, a slight change in damping will affect the system a lot.

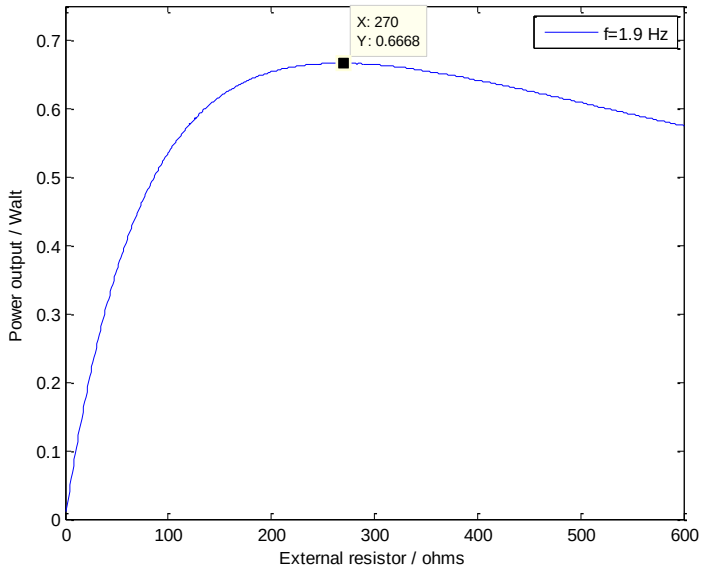

Figure 4-17 relationship between the external resistor and the output power on the external resistor when system is driven under 1.9Hz, 0.5g acceleration

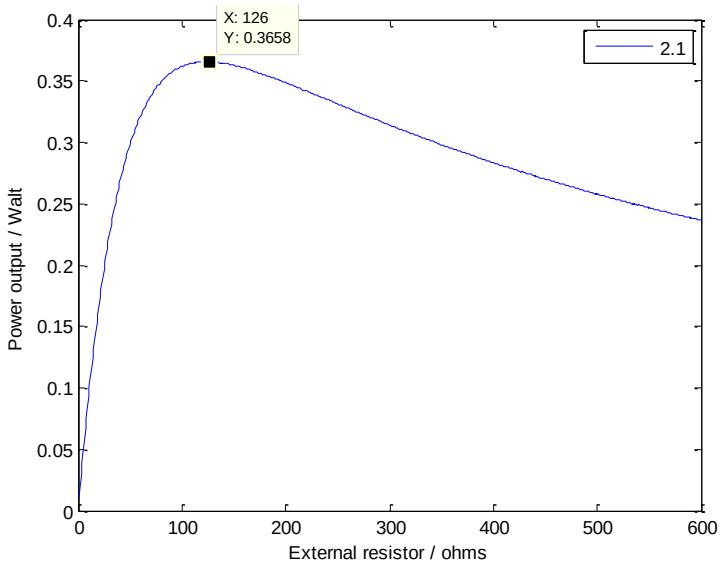

Figure 4-18 relationship between the external resistor and the output power on the external resistor when system is driven under 2.1Hz, 0.5g acceleration

Figure 4-17 and 4-18 shows the relationship between external resistor and the output power on the external resistor when the system is driven under 2Hz and 2.1 Hz. When the system is driven under 1.9 Hz and the external resistor is 270 ohms the output power on it would be maximized at 0.6668 Walt. If the system is driven under 2.1 Hz frequencies, the optimized resistor is changed to 126 Ohms and the peak power output is now 0.3658 Walt. Ideally we need to match the optimized resistor for different frequencies in order to maximize the output power under different driving frequency, but practically we can set the external resistor at a high value, in the case study 200 ohms, for an overall better performance and keep the simplicity at the same time.

4.5.2. Rotational inertia

Another parameter that we can play with to change the performance of MMR-PEH is the added rotational inertia of the motor during engagement. In the case study of section 4.4, the added mass is $m_s = J_g R_b^2 + J_m (R_g R_b)^2 = 2.5488 \times 10^{-4}\ kgm^2$ and the added mass ratio can be calculated as $u = \frac{m_s}{J_\theta} = 17.143\%$. By increasing the rotational inertia of motor rotor J_m, i.e. attach a flywheel to the motor shaft , we can increase the increase the added mass ratio. Replace the added mass m_s with μJ_θ , the dynamic equation of MMR-PEH can be rewritten as:

$$\text{engage: } (1+\mu)J_\theta\ddot{\theta} + (c_e + c_m)\dot{\theta} + MgL\sin\theta = FL$$
$$\text{disengage:}\begin{cases} J_\theta\ddot{\theta} + c_m\dot{\theta} + MgL\sin\theta = FL \\ \mu J_\theta\ddot{\theta}_m + c_e\dot{\theta}_m = 0 \end{cases} \tag{4.34}$$

$\mu = \frac{m_s}{J_\theta}$ is the mass ratio of the added mass over the rotational inertia of the pendulum system.

Increase μ first will introduce more mass in the engaged pendulum system, it will reduce the rotational velocity of the pendulum waving motion if the driven force remains the same. The mass ratio also affects the motion of motor in the period of total disengagement.

The general solution for dynamic motion of disengaged motor system $\mu J_\theta\ddot{\theta}_m + c_e\dot{\theta}_m = 0$ with initial rotational speed $\dot{\theta}_{m0}$ is:

$$\dot{\theta}_m = \dot{\theta}_{m0} \cdot e^{-t/\tau} \tag{4.35}$$

Where τ is the time constant of the decaying defined as:

$$\tau = \frac{\mu J_\theta}{c_e} \tag{4.36}$$

At the instance MMR-PEH get totally disengaged, the motor inertia and the electrical damping will be removed from the system, motor system starts decaying its rotational speed with an inertial speed $\dot{\theta}_{m0}$ and the decaying is related with time constant τ. If the system get a constant electrical damping, with larger mass ratio μ, the motor will decay in a slower speed. The change of time constant will affect the engage and disengage time of the system, also the average rotational speed of the motor system.

The disengage system will not change because of the mass ratio μ, however it will affect the natural frequency of engaged pendulum system, shown in equation(4.37):

$$f_{engage} = \frac{1}{2\pi\sqrt{MgLJ_\theta(1+\mu)}} \tag{4.37}$$

Increase the mass ratio μ will reduce the natural frequency of engaged system, increase the gap between the natural frequencies of engage system and disengage system. The properties of the system due to nonlinearity of switched system will also be enlarged.

In the next studies, we keep all the parameters same as in table 4-1 except that we added an extra rotational inertia to the motor shaft, the system is still being driven under a 0.5g amplitude sinusoids external force. If the mechanical damping and electrical damping in the system doesn't change while the mass ratio is increase, the damping ratio of the system will decrease, this will also affect the performance of MMR-PEH.

In order to study the influence, we run the simulation with different mass ratio of 0.5, 0.8 and 1.0, shown in table 4-2. For time domain plot, the system is driven under the 3Hz sinusoid excitation, the acceleration is set as 0.5g.

Table 4-2 parameters to study the influence of mass ratio

Motor inertia J_m	Mass ratio μ	Engaged natural frequency f_{engage}
$38 gcm^2$	0.501	1.5820 Hz
$61 gcm^2$	0.804	1.4430 Hz
$78 gcm^2$	1.028	1.3609

4.5.2.1. Comparison of time domain signal

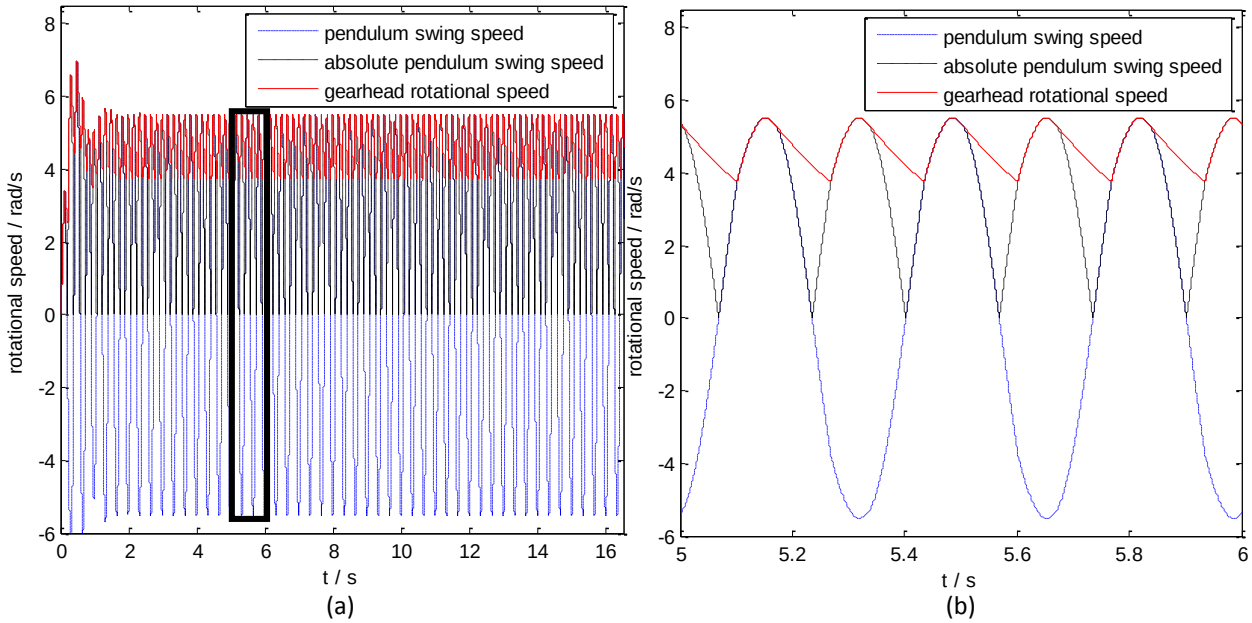

Figure 4-19 Time domain signal output of MMR-PEH when u=0.5, driven under 0.5g acceleration

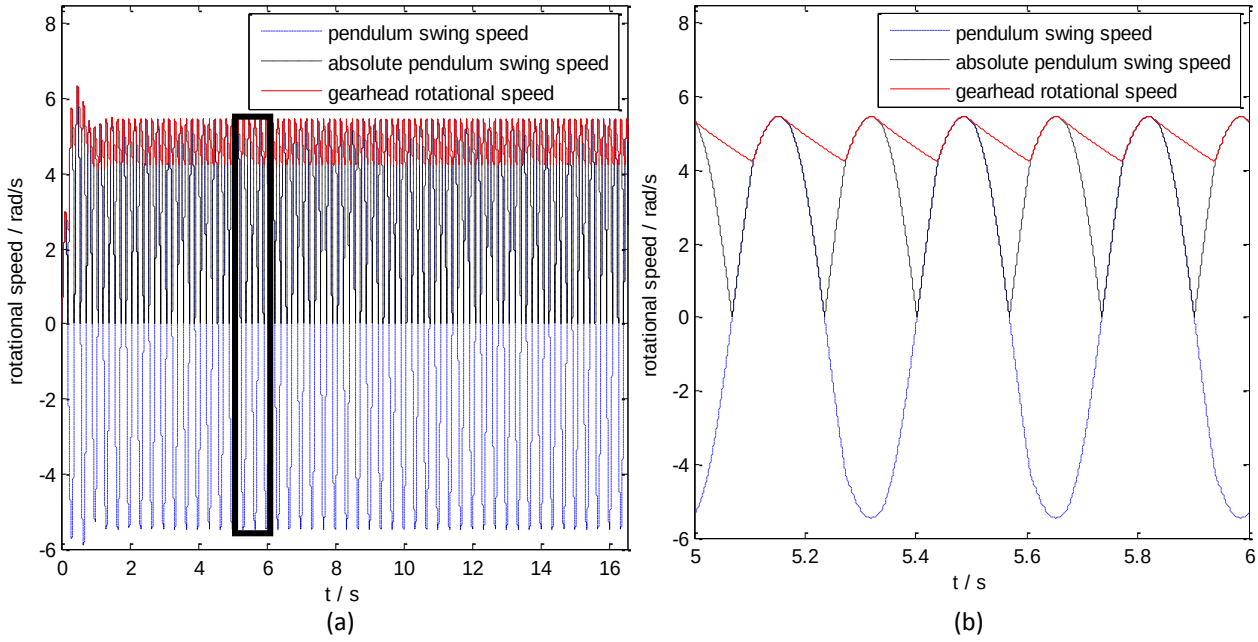

Figure 4-20 Time domain signal output of MMR-PEH when u=0.8, driven under 0.5g acceleration

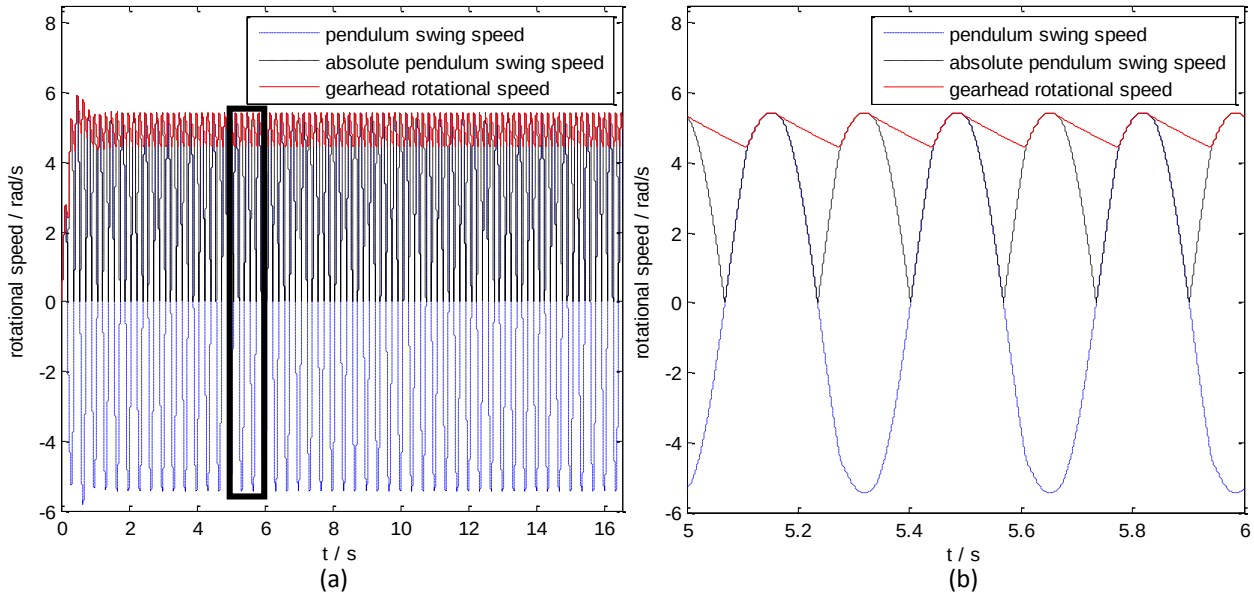

Figure 4-21 Time domain signal output of MMR-PEH when u=1.0, driven under 0.5g acceleration

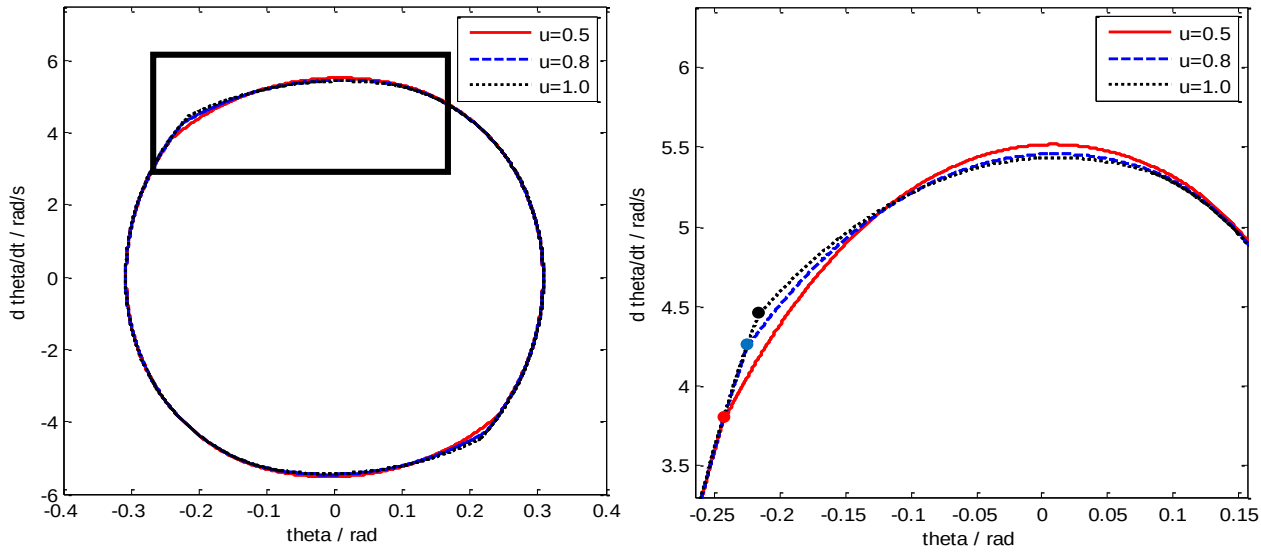

Figure 4-22 Phase portrait of pendulum motion with different mass ratio, driven under 0.5g acceleration

Figure 4-22 shows the phase portrait of pendulum motion during stable period. From zoomed in figure, the peak swing speed of the pendulum didn't change much with the increase of added mass ratio. There is a sharp corner on the phase portrait, marked as black blue and red dot, they represent the instance MMR-PEH systems with different mass ratio switch from disengage to engage. The added mass at this instance, connected with the pendulum system and changed the dynamics of the pendulum system.

Figure 4-19 to 4-21 shows the time domain signals of the MMR-PEH with different mass ratio. Since the driving frequency is 3 Hz, after the transient period, the MMR-PEH systems become stable and the output frequency is settle down to be same as the driving frequency. With the increase of mass ratio, the time constant τ which is described in equation (4.36) increases. The increase of time constant means that the slower reduce on the velocity once the motor system get an initial speed. Because the peak value of the pendulum swing motion didn't change much with the change of mass ratio, larger mass ratio means the motor system maintains an overall higher velocity. Also the percentage time of the system staying in total disengage period will be increased with the increase of mass ratio.

4.5.2.2. Comparison of frequency response

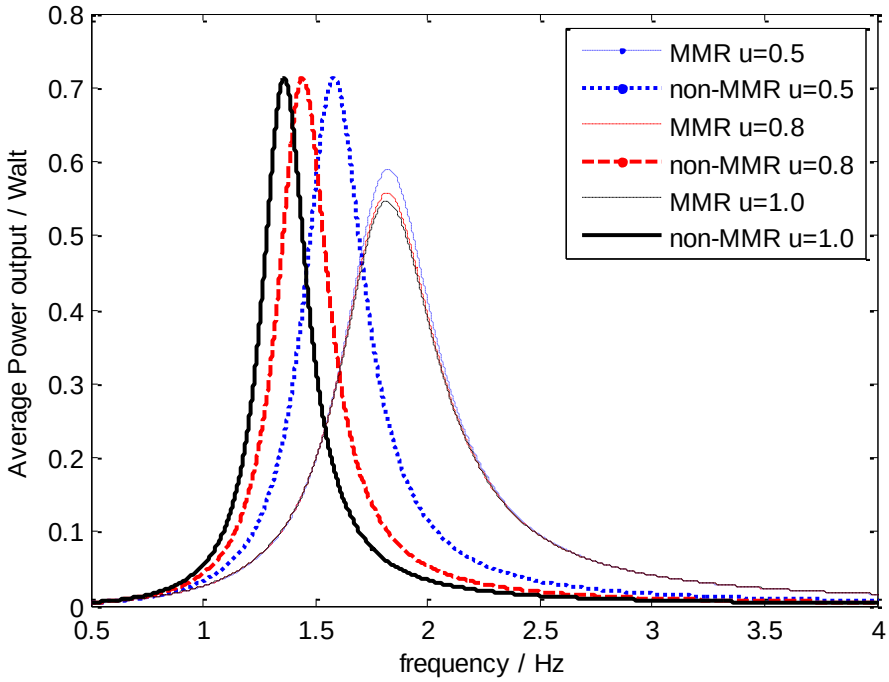

Figure 4-23 Frequency response of MMR-PEH and non-MMR-PEH with different mass ratio, driven under 0.5g acceleration

Figure 4-23 shows the frequency response of MMR-PEH and non-MMR-PEH with different mass ratio. With the increase of mass ratio, the natural frequency of the non-MMR-PEH shift a lot while the MMR-PEH didn't change much. Which means the natural frequency of non-MMR-PEH is sensitive to the change of mass while the MMR-PEH is not. The peak power on the

MMR-PEH is decreased however it achieved a broader bandwidth. Introduce the same method for judging the bandwidth of frequency response as figure 4-13, $\frac{peak\ value}{\sqrt{2}}$ is chosen as the judging criteria to calculate the crossing frequency at that power level.

Table 4-3 shows the detailed parameters calculated from the frequency response of MMR-PEH vs non-MMR-PEH with different mass ratio. As was shown in the table, when the mass ratio is 0.17, compared with non-MMR, the MMR has 5% decrease on the peak power however it achieved 19% increase on the cross frequency. When the mass ratio is 1.0, the peak power is decreased by 24% however it achieved 2.17 times the cross frequency than non-MMR system. We can draw conclusion that MMR-PEH has a tradeoff between higher peak power at its natural frequency and broader bandwidth.

Table 4-3 parameters in frequency response with change of mass ratio

Mass ratio μ	Peak power (Walt)			Cross frequency (Hz)			Peak power/natural frequency		Average power over frequency (Walt)		
	MMR	Non-MMR	Ratio	MMR	Non-MMR	Ratio	MMR	Non-MMR	MMR	Non-MMR	ratio
0.17	0.6781	0.7132	0.9508	0.32	0.27	1.19	1.85	1.79	0.0804	0.0753	1.0677
0.5	0.5899	0.7133	0.8270	0.328	0.212	1.55	1.823	1.582	0.0746	0.0594	1.2559
0.8	0.558	0.7133	0.7823	0.339	0.177	1.92	1.822	1.443	0.0727	0.0498	1.4598
1.0	0.5469	0.7133	0.7667	0.343	0.158	2.17	1.820	1.361	0.0721	0.0444	1.6239

If we track the natural frequency of MMR-PEH and non-MMR-PEH with the change of mass ratio, we can find that when the mass ratio u is changed from 0.17 to 1.0, the natural frequency of MMR changed by 0.03 Hz however the non-MMR system changed a lot which is 0.43 Hz. Which means the MMR-PEH system is not sensitive to the change of system mass. This property may have some unique applications for some special problems.

The average power over frequency represents the area of the frequency response plot, the physical meaning of the area is the system power output driven by a white noise, the bigger area the better. We can see that with the increase of mass ratio, the average power over frequency of MMR-PEH didn't change much however the non-MMR-PEH decreased a lot. At the case when $\mu = 1$, the area of MMR-PEH is 62.4% larger than non-MMR-PEH, making it huge advantage if the system is driven under white noise or the excitation signal contains a lot of frequency components.

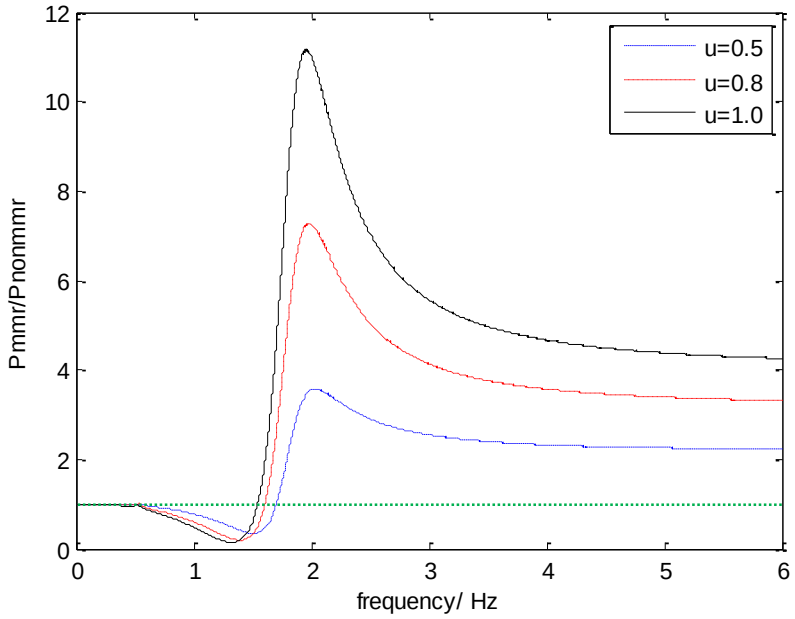

Figure 4-24 Power ratio between MMR-PEH and non-MMR-PEH with different mass ratio vs driving frequency , driven under 0.5g acceleration

Figure 4-24 shows the influence of mass ratio on the power output ratio of MMR-PEH over non-MMR-PEH vs driving frequency. Power ratio equal "1", marked as green dot line, means the power output from MMR-PEH is same as non-MMR-PEH. At lower frequency, non-MMR-PEH have advantage over the MMR-PEH, however when the driving frequency becomes higher, MMR-PEH will always have advantage over the non-MMR-PEH and it will settle down to a certain number. The larger mass ratio is, the higher this settled number will be.

4.5.2.3. A typical case when the MMR-PEH system has large mechanical damping

In the previous analysis, the mechanical damping ratio of the pendulum is set to be an constant number $\xi_m = 0.05$. If the system has a higher mechanical damping and large added mass, the MMR-PEH system will gain a huge advantage over the non-MMR-PEH system.

Set the system parameters same as table 4-1, except for that the mechanical damping $c_m = 0.006$ (15% mechanical damping ratio) and the rotational inertia of motor is $114 gcm^2$. The external resistor is $R = 80\Omega$. The external driving force is still set to be 0.5g, 3Hz, sinusoid.

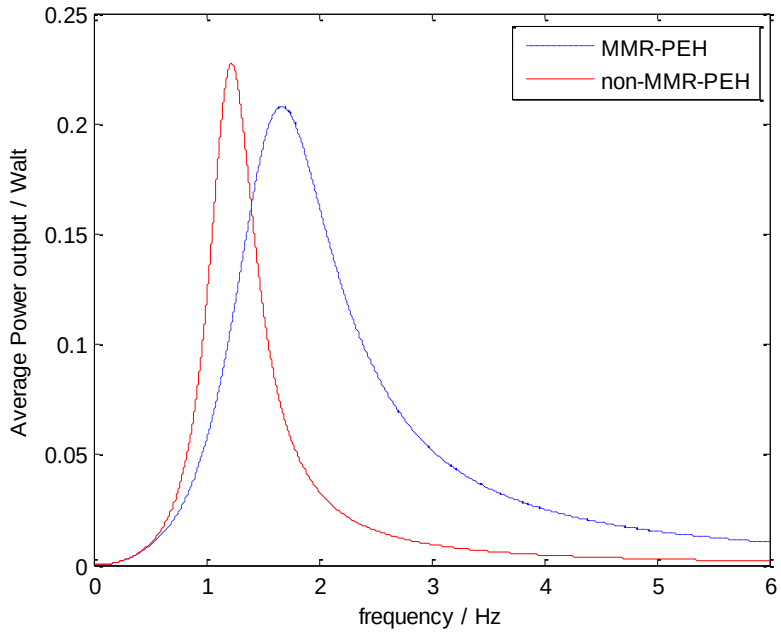

Figure 4-25 Frequency response of MMR-PEH and non-MMR-PEH under high mechanical damping and large mass ratio, driven under 0.5g acceleration

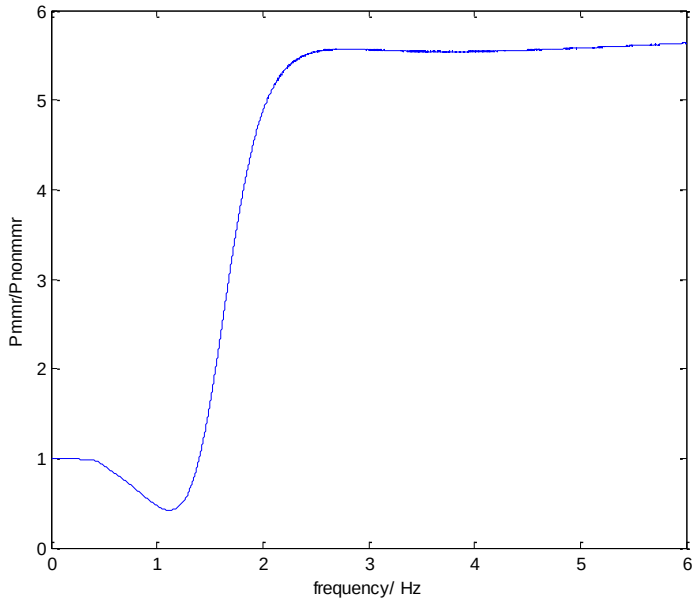

Figure 4-26 Power ratio between MMR-PEH and non-MMR-PEH vs driving frequency under high mechanical damping and large mass ratio, driven under 0.5g acceleration

Figure 4-25 and 4-26 shows the frequency response of MMR-PEH and non-MMR-PEH under high mechanical damping.

Table 4-4 parameters in frequency response of MMR-PEH and non-MMR-PEH under high mechanical damping and large mass ratio

Mass ratio μ	Peak power (Walt)			Cross frequency (Hz)			Peak power/natural frequency		Average power over frequency (Walt/Hz)		
	MMR	Non-MMR	Ratio	MMR	Non-MMR	Ratio	MMR	Non-MMR	MMR	Non-MMR	ratio
1.5	0.2081	0.2272	0.9159	0.735	0.335	2.194	1.674	1.225	0.0558	0.0292	1.9110

Table 4-4 shows the parameters in the frequency response. The peak power of MMR-PEH dropped 8.41% however it achieved 2.19 times the cross frequency and 1.91 times the average power over frequency. Under this condition, MMR-PEH gains huge advantage over the non-MMR-PEH system.

In this section we case studied a prototype of MMR-PEH about its performance. Compared with always engaged single DOF non-MMR-PEH, the MMR-PEH can harvester more energy in higher frequency above the natural frequency of non-MMR-PEH. MMR-PEH has disadvantage when the system is driven under single frequency since the peak on the frequency response is lower than non-MMR-PEH system, but it achieved a broader bandwidth frequency response. When the driving force is a white noise, or contains a broad frequency elements, the MMR-PEH will have a greater power output than non-MMR-PEH.

4.6. Experimental verification

Experimental verification for the comparison between a MMR-PEH and a non-MMR-PEH is proposed in this section. Time domain signal from MMR-PEH and non-MMR-PEH as well as the average power output vs driving frequency is shown. The experimental result provide that the MMR-PEH can harvest more energy than non-MMR-PEH at certain frequencies above natural frequency.

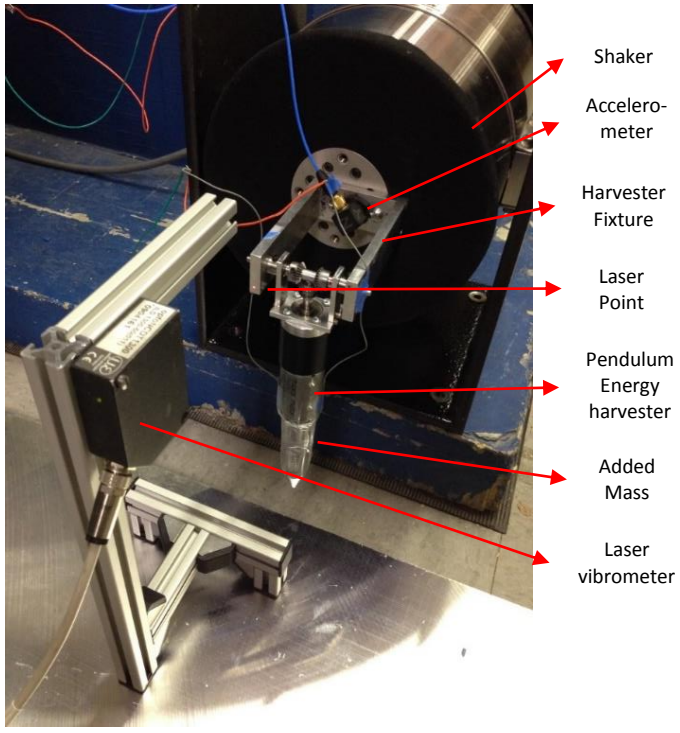

Figure 4-27 Experimental setup

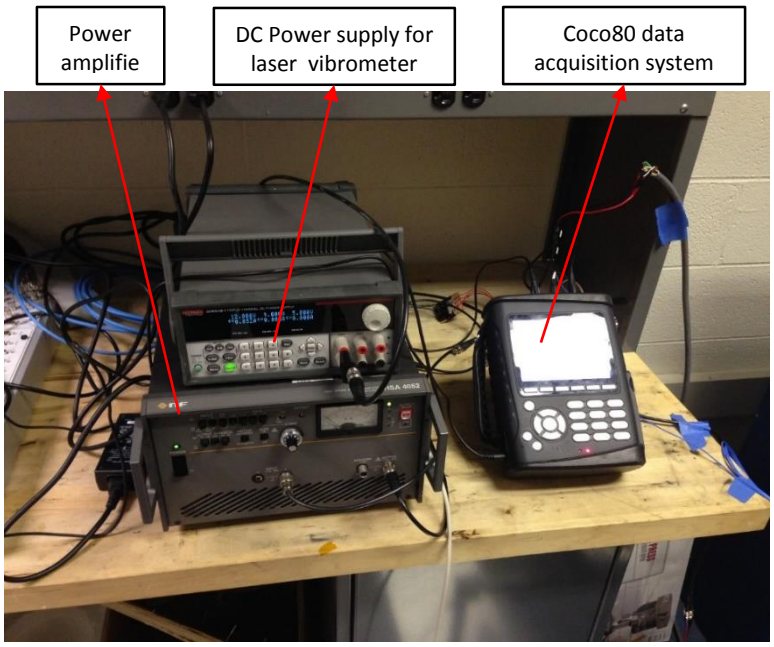

Figure 4-28 power supply and data acquisition system for the experiment

Figure 4-27 and 4-28 shows the experimental setup, power supply and data acquisition for MMR-PEH and non-MMR-PEH test. A VTS VC 100-6 shaker is used to drive the system. The pendulum energy harvester is rigid connected to the base of the shaker by a u-shaped fixture. A maxon RE-max29 9W motor with a GP32A 14:1 gear head is used as a generator for the system. A PCB 356A17 3 axial accelerometer and a Micro-Epsilon optoNCDT 1300 laser vibrometer are used to measure the acceleration and displacement of the system. A coco-80 dynamic signal analyzer is used to give excitation source, acquire the signal from laser vibrometer, accelerometer and the output from the energy harvester. A NF HAS 4052 high speed bipolar amplifier is used to amplify the excitation source from the dynamic signal analyzer to drive the shaker. A KEITHLEY 2230G-30-1 triple channel DC power supply is used to power the laser vibrometer.

In the test, the dynamic signal analyzer generates a low voltage sinusoid source signal with desired frequency, this signal will be enlarged by the power amplifier to power the shaker. The shaker drives the MMR-PEH or non-MMR-PEH system at set frequency, at the same time the vibrometer and accelerometer measures the displacement and acceleration of the shaker. Finally the signal from vibrometer, accelerometer and the output voltage from the energy harvester is recorded on the dynamic signal analyzer. Based on the loading of the energy harvester, the RMS value of the output voltage, the driving frequency and the driving amplitude (displacement and

acceleration), we can normalize the corresponding power output from the energy harvester at certain frequency. Repeat the tests on both MMR-PEH and non-MMR-PEH we can compare the performance of MMR-PEH and non-MMR-PEH at frequency domain.

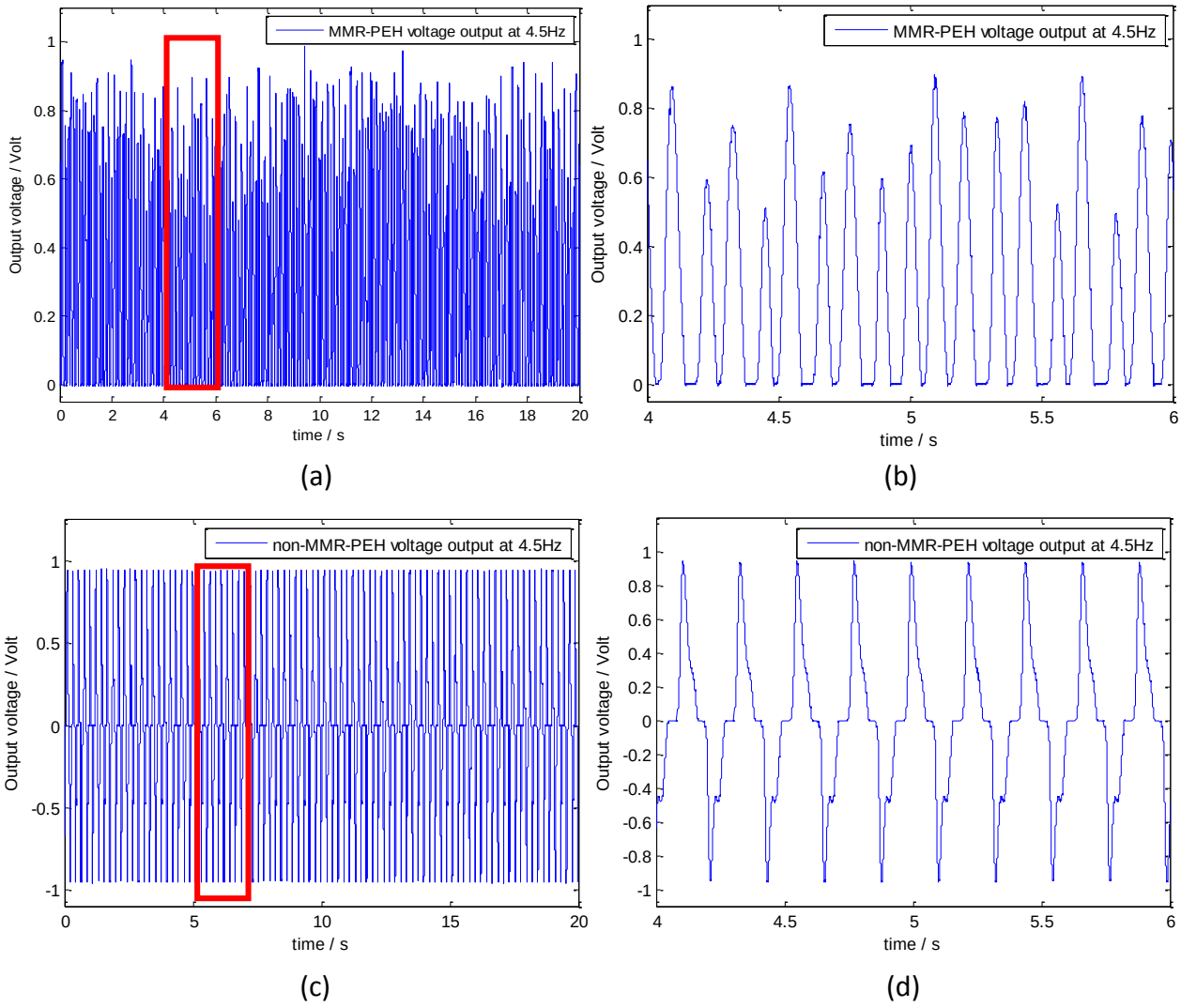

Figure 4-29 Time domain voltage output from MMR-PEH and non-MMR-PEH with 40 ohms load and driven at 4.5 Hz (a)voltage output from MMR-PEH(b) zoomed in voltage output from MMR-PEH (c) voltage output from non-MMR-PEH (d) zoomed in voltage output from non-MMR-PEH

A typical time domain signal output from a MMR-PEH and a non-MMR-PEH is shown in figure 4-29. The system is driven under a 4.5 Hz sinusoid source and the voltage output from the MMR-PEH is a regulated DC source while the voltage output from the non-MMR-PEH is an AC source. Both of the energy harvester are affected by the backlash and get a certain period with 0

voltage output during the excitation. The peak voltage output from non-MMR-PEH is at the same level however the MMR-PEH voltage peak is changing in a small range.

There are two problems need to be pointed out since the experiment result is different from the result we got in simulation (figure 4-11). The first problem is the peak voltage from the MMR-PEH, presented in figure 4-29 (b), is always changing along with time. One of the potential reasons for this phenomenon is friction. Ideally the pendulum should wave symmetrically along an equilibrium position under sinusoid excitation, because the gravity of the pendulum is acting as a spring which will drive the pendulum system back to its equilibrium position once it's forced to shift from the equilibrium position. However, the friction in the system, typically in bearing and miter gear, will cancel the gravitational force within a certain range. Therefore within this small angle all the positions are potential equilibrium position for the pendulum system since the gravitational force is counteracted with friction. An uncertainty is introduced into the pendulum system that's why the peak is always changing. The observation of the experiment matches with this theory: the pendulum never settle down to a certain position when given high frequency excitation, the equilibrium position is always changing within a certain small angle.

Another problem is that there are several flat surface at the bottom of the voltage output, shown in figure 4-28 (b), which means that there will be no voltage output from the MMR-PEH during this time. This is very different from the simulation result we got previously. Voltage output from the energy harvester is proportional to the rotational velocity on the motor shaft. Theoretically when the rotational speed on the motor shaft is lower than the waving velocity of the pendulum, the system will switch from total disengage to engage and the motor will again rotate along with the pendulum. The velocity of the motor shaft is then kept higher than zero. However, because of the small backlash of the miter gear in the transmission, there will be a transient period when the direction of the pendulum waving velocity is changed. This transient zero velocity time is highly related with the driving frequency. At lower frequency this transient period is longer than at higher frequency since the average velocity of the system at low frequency is slower.

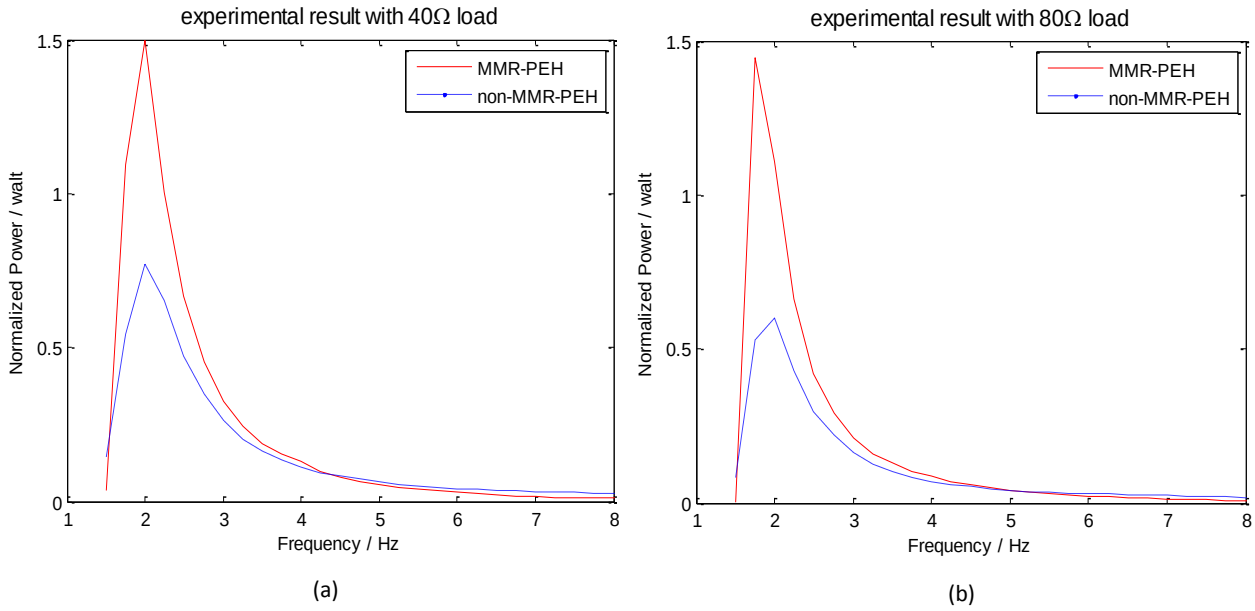

Figure 4-30 Averaged power output vs driving frequency (a) with 40 ohms load and (b) with 80 ohms load

Figure 4-23 shows the frequency response of MMR-PEH and non-MMR-PEH with different external loads. The input force to the system is proportional to the acceleration and the output power is thus proportional to the acceleration square. In order to put in fair comparison for both systems and keep consistent with the simulation result (in simulation we use same acceleration to drive the system at different frequencies), the power output of both MMR-PEH and non-MMR-PEH are normalized to the same acceleration 1.2g.

The natural frequency is 1.8Hz for non-MMR-PEH system and around 1.9Hz for MMR-PEH, in simulation the power output from MMR-PEH is a little smaller than non-MMR-PEH at natural frequency and will always better than MMR-PEH. However, the result we got from experiment is somehow different. The normalized power output from MMR-PEH is dominating over the non-MMR-PEH when the frequency is under 4.3Hz for 40 ohms load and 5Hz for 80 ohms load and after this frequency, the performance of MMR-PEH is always worse than non-MMR-PEH. The explanation for this phenomenon can be explained as this: the limitation of the equipment and backlash lead to the bad performance for non-MMR-PEH in low frequency while the backlash and friction reduced the function of MMR-PEH at high frequency.

The driving force to the system is proportional to the acceleration on the shaker, acceleration is proportional to square of the driving frequency. Since the maximum displacement

the shaker can provide is very limited, at low frequency below 1.5 Hz the shaker can't give enough force to drive the system. Therefore we can barely get any power output from both the MMR-PEH and non-MMR-PEH at lower frequency. And we missed the key frequency where non-MMR-PEH should perform better than the MMR-PEH. That's why we can't get demonstrate the simulation well for MMR-PEH in low frequency.

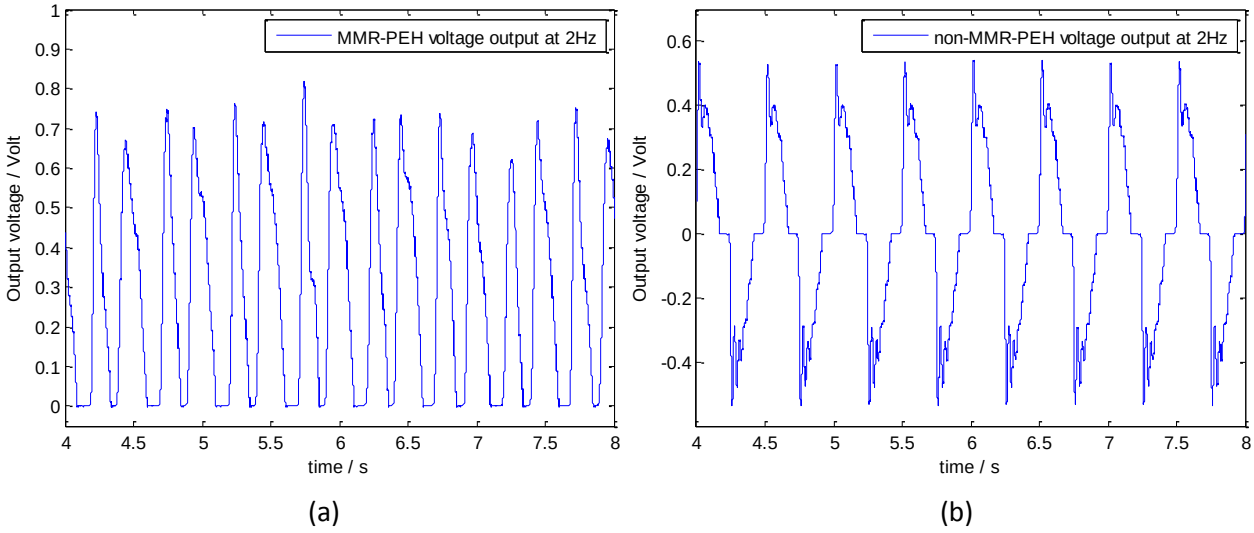

Figure 4-31 Time domain voltage output 40 ohms load and driven at 2Hz (a) MMR-PEH (b) non-MMR-PEH

Another problem caused the bad performance of non-MMR-PEH at low frequency is backlash. Figure 4-31 shows the voltage output of both systems driven at 2Hz with 40 ohms load. Though both systems have a period with zero voltage output due to the backlash, non-MMR-PEH, however, have longer zero output time in one period than the MMR. This is because for non-MMR-PEH system, only one pair of miter gears are used for transmit the motion. When the pendulum wave back and force, this transmission direction changed accordingly. Therefore, the backlash between the gears will cause discontinuity in the output motion of the non-MMR-PEH. It will introduce impact in the motion and also reduce the power output from the non-MMR-PEH. However for the MMR-PEH three gears are used to transmit the motion and for each gear the rotational direction is always same. There will still be backlash during the transmission of MMR-PEH in gear box and the misalignment of the three gears but the influence will be smaller. That's why at low frequency non-MMR-PEH will have longer zero output time than the MMR-PEH. The longer zero output time will also lower the peak output voltage of non-MMR-PEH and causing the dominating performance of MMR-PEH over non-MMR-PEH at low frequency.

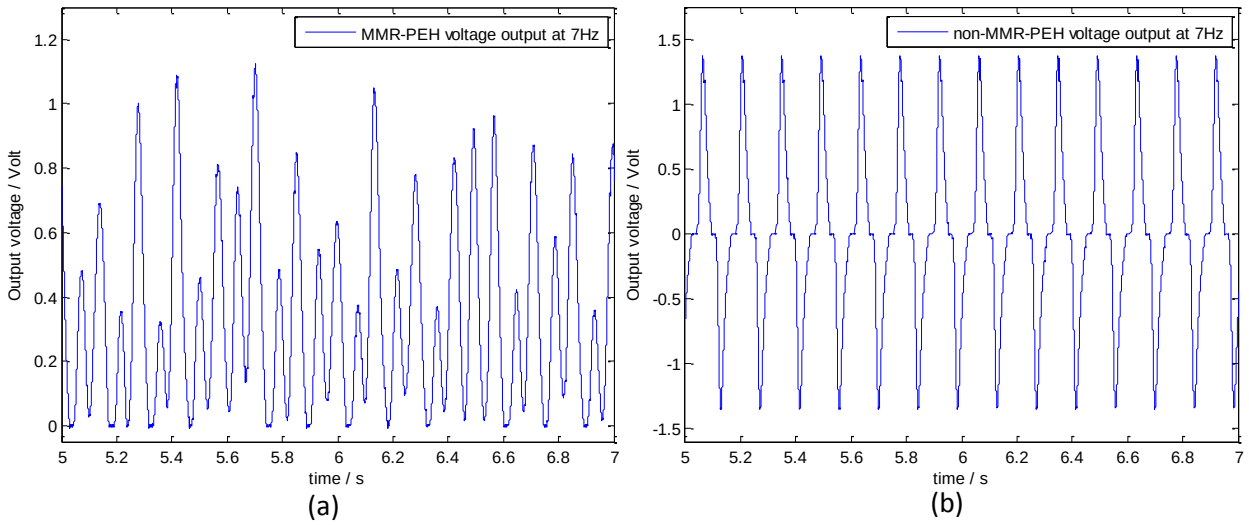

Figure 4-32 Time domain voltage output 40 ohms load and driven at 7Hz (a) MMR-PEH (b) non-MMR-PEH

In higher frequency, however, is a different story. Figure 4-32 shows time domain voltage output of both systems with 40 ohms load and driven at 7Hz. For non-MMR-PEH, because the two miter gears are always engaged, the overall length of backlash is set. When the frequency becomes higher, the rotational speed of the gears are increasing, which will reduce the time the system to overcome the backlash. Compared with figure 4-32 (b) and 4-32 (b), we can clearly see that the transient time for the non-MMR-PEH is reduced and the peak voltage is increased. For MMR-PEH, as we mentioned in the previous paragraph, the equilibrium position for the pendulum system is always changing due to the friction and backlash. When the excitation frequency is low it didn't affect the system much, however when the driving frequency keeps increasing the effect of nonlinearity become larger. Compared with figure 4-32 (a) and 4-32 (a), fluctuate of the peak voltage is much more severe, although some of the peak voltage is higher than the lower frequency ones with the increase of frequency and the voltage output is always larger zero, but the average power output from the MMR-PEH is reduced.

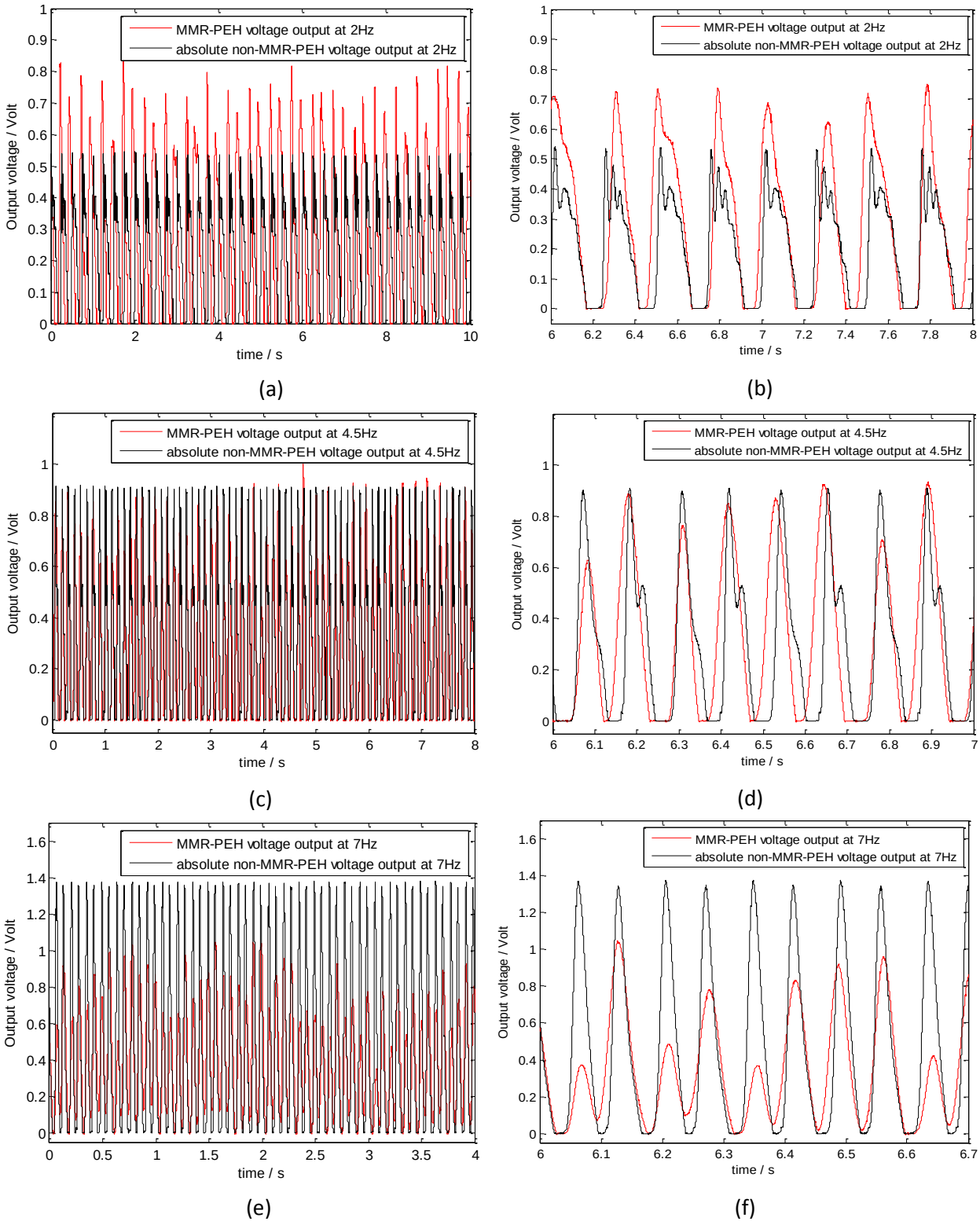

Figure 4-33 Comparison between the voltage output from MMR-PEH and the absolute voltage output from non-MMR-PEH at 2Hz, 4.5Hz and 7Hz

Figure 4-33 shows the comparison between the voltage output from MMR-PEH and the absolute voltage output from non-MMR-PEH at different driving frequencies. Since the voltage output from non-MMR-PEH is an AC source, in order to directly compare the performance of MMR-PEH and non-MMR-PEH, we need to take the absolute value of the non-MMR-PEH. In practice, the non-MMR-PEH requires a full wave bridge rectifier to rectify the ac source into a dc source because we can only directly store the DC power. The diode in the rectifier circuit will cause voltage drop during the rectify processing, also reduced the power output from the non-MMR-PEH. The voltage may drop 0.2 to 0.4 volt per diode the voltage went through, this is a huge disadvantage for non-MMR-PEH. However in both experiment and simulation we didn't take this voltage drop into account.

In the comparison between the voltage of MMR-PEH and non-MMR-PEH, we can see that at 2Hz, MMR-PEH has a higher voltage peak and less zero voltage period. At 4.5 Hz the performance of non-MMR-PEH and MMR-PEH are very close. When the excitation frequency hit 7 Hz, the peak of MMR-PEH becomes unstable and non-MMR-PEH has a better performance at this time. The time domain results matches well with the frequency response we got previously.

In conclusion, due to the backlash, limitation of experimental equipment and friction, we can't well demonstrate the simulation result we got. However the experiment shows that MMR-PEH has the potential to have better performance than non-MMR-PEH at certain frequency over natural frequency.

5. Conclusion

In this thesis, a multi-source energy harvester based wildlife tracking collar is proposed which can largely extend the duration of the wildlife tracking system. A feedforward and feedback control based dc-dc boost converter is demonstrated to have a better performance of tracking the maximum power point on a solar panel. Simulation result was demonstrated and showed that the proposed circuit can achieve the MPPT performance autonomously. A novel electromagnetic rotational pendulum energy harvester with mechanical motion regulator is proposed, which can mechanically rectify the bidirectional waving motion of a pendulum into a unidirectional rotational motion of a motor. Therefore we can get rid of the full bridge rectifier circuit to achieve higher efficiency. The nonlinearity of one-way clutch can protect the energy harvester with large impact and also enhance a broad bandwidth frequency response for the pendulum energy harvester. Dynamic modeling and simulation results is shown and the switch linear performance is established. Experiment result confirmed that the proposed pendulum energy harvester can achieve better performance over the traditional rigid connected energy harvester at certain frequency over natural frequency.

Reference

1. Cagnacci, F., et al., *Animal ecology meets GPS-based radiotelemetry: a perfect storm of opportunities and challenges.* Philosophical Transactions of the Royal Society B-Biological Sciences, 2010. **365**(1550): p. 2157-2162.
2. Bridge, E.S., et al., *Technology on the Move: Recent and Forthcoming Innovations for Tracking Migratory Birds.* Bioscience, 2011. **61**(9): p. 689-698.
3. Block, B.A., et al., *Electronic tagging and population structure of Atlantic bluefin tuna.* Nature, 2005. **434**(7037): p. 1121-1127.
4. Arnemo, J.M., Evans, A., & Fahlman, Å., *Biomedical protocols for free-ranging brown bears, gray wolves, wolverines and lynx.* Hedmark University College. Evenstad, Norway, 2011.
5. Cattet, M., et al., *An evaluation of long-term capture effects in ursids: Implications for wildlife welfare and research.* Journal of Mammalogy, 2008. **89**(4): p. 973-990.
6. Salas, V., et al., *Review of the maximum power point tracking algorithms for stand-alone photovoltaic systems.* Solar Energy Materials and Solar Cells, 2006. **90**(11): p. 1555-1578.
7. Lowe, R.A., G. A. Landis, and P. Jenkins, *The efficiency of photovoltaic cells exposed to pulsed laser light.* 1993.
8. Phang, J.C.H., D.S.H. Chan, and J.R. Phillips, *Accurate Analytical Method for the Extraction of Solar-Cell Model Parameters.* Electronics Letters, 1984. **20**(10): p. 406-408.
9. Khatib, T.T.N., et al., *An efficient maximum power point tracking controller for photovoltaic systems using new boost converter design and improved control algorithm.* WSEAS Trans. Power Syst., 2010. **5**(no.2): p. 55-63.
10. Nishioka, K., et al., *Analysis of the temperature characteristics in polycrystalline Si solar cells using modified equivalent circuit model.* Japanese Journal of Applied Physics Part 1-Regular Papers Short Notes & Review Papers, 2003. **42**(12): p. 7175-7179.
11. Hamdy, M.A., *A New Model for the Current-Voltage Output Characteristics of Photovoltaic Modules.* Journal of Power Sources, 1994. **50**(1-2): p. 11-20.
12. Chen, Y., et al., *A new maximum power point tracking controller for photovoltaic power generation.* Apec 2003: Eighteenth Annual Ieee Applied Power Electronics Conference and Exposition, Vols 1 and 2, 2003: p. 58-62.
13. Jiang, J., et al., *Maximum power tracking for photovoltaic power systems.* Tamkang Journal of Science and Engineering, 2005(8(2)): p. 147.
14. Ibrahim, H.S., et al., *Microcomputer controlled buck regulator for maximum power point tracker for DC pumping system operates from photovoltaic system.* In Fuzzy Systems Conference Proceedings, 1999. **1**(406-411).
15. Salameh, Z. and D. Taylor, *Step-up Maximum Power Point Tracker for Photovoltaic Arrays.* Solar Energy, 1990. **44**(1): p. 57-61.
16. de Cesare, G., D. Caputo, and A. Nascetti, *Maximum power point tracker for portable photovoltaic systems with resistive-like load.* Solar Energy, 2006. **80**(8): p. 982-988.
17. Lim, Y.H. and D.C. Hamill, *Simple maximum power point tracker for photovoltaic arrays.* Electronics Letters, 2000. **36**(11): p. 997-999.

18. Xiao, W.D. and W.G. Dunford, *A modified adaptive hill climbing MPPT method for photovoltaic power systems.* Pesc 04: 2004 Ieee 35th Annual Power Electronics Specialists Conference, Vols 1-6, Conference Proceedings, 2004: p. 1957-1963.
19. Femia, N., et al., *Optimization of perturb and observe maximum power point tracking method.* Ieee Transactions on Power Electronics, 2005. **20**(4): p. 963-973.
20. B.K.Bose, P.M.Szczesny, and R.L.Steigerwald, *Microcomputer Control of a Resi-dential Photovoltaic Power Condictioning System.* IEEE Trans. on Industry Applications, 1985. **IA-21**(no. 5): p. 1182~1191.
21. Sullivan, C.R. and M.J. Powers, *A High-Efficiency Maximum Power Point Tracker for Photovoltaic Arrays in a Solar-Powered Race Vehicle.* Pesc 93 Record - 24th Annual Ieee Power Electronics Specialists Conference, 1993: p. 574-580.
22. Hohm, D.P. and M.E. Ropp, *Comparative study of Maximum Power Point Tracking algorithms using an experimental, programmable, maximum power point tracking test bed.* Conference Record of the Twenty-Eighth Ieee Photovoltaic Specialists Conference - 2000, 2000: p. 1699-1702.
23. Koutroulis, E., K. Kalaitzakis, and N.C. Voulgaris, *Development of a microcontroller-based, photovoltaic maximum power point tracking control system.* Ieee Transactions on Power Electronics, 2001. **16**(1): p. 46-54.
24. Subudhi, B. and R. Pradhan, *A Comparative Study on Maximum Power Point Tracking Techniques for Photovoltaic Power Systems.* Ieee Transactions on Sustainable Energy, 2013. **4**(1): p. 89-98.
25. Salas, V., et al., *Evaluation of a new maximum power point tracker applied to the photovoltaic stand-alone systems.* Solar Energy Mater. Solar Cells, 2005. **87**(no.1-4): p. 807-815.
26. Hua, C.C. and C.M. Shen, *Study of maximum power tracking techniques and control of DC/DC converters for photovoltaic power system.* Pesc 98 Record - 29th Annual Ieee Power Electronics Specialists Conference, Vols 1 and 2, 1998: p. 86-93.
27. Maheshappa, H.D., J. Nagaraju, and M.V.K. Murthy, *An improved maximum power point tracker using a step-up converter with current locked loop.* Renewable Energy, 1998. **13**(2): p. 195-201.
28. Hua, C.C. and C.M. Shen, *Comparative study of peak power tracking techniques for solar storage system.* Apec '98 - Thirteenth Annual Applied Power Electronics Conference and Exposition, Vols 1 and 2, 1998: p. 679-685.
29. Rahimi, A., et al., *Fully Self-Powered Electromagnetic Energy Harvesting System With Highly Efficient Dual Rail Output.* Ieee Sensors Journal, 2012. **12**(6): p. 2287-2298.
30. Roundy, S. and E. Takahashi, *A planar electromagnetic energy harvesting transducer using a multi-pole magnetic plate.* Sensors and Actuators a-Physical, 2013. **195**: p. 98-104.
31. Rahimi, A., et al., *An electromagnetic energy harvesting system for low frequency applications with a passive interface ASIC in standard CMOS.* Sensors and Actuators a-Physical, 2012. **188**: p. 158-166.
32. Wang, D.A., C.Y. Chiu, and H.T. Pham, *Electromagnetic energy harvesting from vibrations induced by Karman vortex street.* Mechatronics, 2012. **22**(6): p. 746-756.

33. Dayal, R., S. Dwari, and L. Parsa, *A New Design for Vibration-Based Electromagnetic Energy Harvesting Systems Using Coil Inductance of Microgenerator.* Ieee Transactions on Industry Applications, 2011. **47**(2): p. 820-830.
34. Yang, B., et al., *Electromagnetic energy harvesting from vibrations of multiple frequencies.* Journal of Micromechanics and Microengineering, 2009. **19**(3).
35. D, M., S. E, and S. M, *Electromagnetic generators employing planar inductors for autonomous sensor applications.* Procedia Chemistry, 2009(1:4): p. 69-72.
36. Tang, L.H., Y.W. Yang, and C.K. Soh, *Toward Broadband Vibration-based Energy Harvesting.* Journal of Intelligent Material Systems and Structures, 2010. **21**(18): p. 1867-1897.
37. Zuo, L., et al., *Design and characterization of an electromagnetic energy harvester for vehicle suspensions.* Smart Materials & Structures, 2010. **19**(4).
38. Gu, L. and C. Livermore, *Passive self-tuning energy harvester for extracting energy from rotational motion.* Applied Physics Letters, 2010. **97**(8).
39. Stanton, S.C., C.C. McGehee, and B.P. Mann, *Reversible hysteresis for broadband magnetopiezoelastic energy harvesting.* Applied Physics Letters, 2009. **95**(17).
40. Stanton, S.C., C.C. McGehee, and B.P. Mann, *Nonlinear Dynamics for Broadband Energy Harvesting: Investigation of a Bi-stable Piezoelectric Inertial Generator.* Physica D, 2010(239): p. 640-653.
41. Ferrari, M., et al., *Improved energy harvesting from wideband vibrations by nonlinear piezoelectric converters.* Sensors and Actuators a-Physical, 2010. **162**(2): p. 425-431.
42. Challa, V.R., M.G. Prasad, and F.T. Fisher, *Towards an autonomous self-tuning vibration energy harvesting device for wireless sensor network applications.* Smart Materials & Structures, 2011. **20**(2).
43. Arrieta, A.F., et al., *A Piezoelectric Bi-stable Plate for Nonlinear Broadband Energy Harvesting.* Applied Physics Letters, 2010(97): p. 104102.
44. Mann, B.P. and N.D. Sims, *Energy harvesting from the nonlinear oscillations of magnetic levitation.* Journal of Sound and Vibration, 2009. **319**(1-2): p. 515-530.
45. Mann, B.P. and B.A. Owens, *Investigations of a Nonlinear Energy Harvester with a Bi-stable Potential Well.* Journal of Sound and Vibration, 2010(329): p. 1215-1226.
46. Wang, Y.J., C.D. Chen, and C.K. Sung, *Design of a frequency-adjusting device for harvesting energy from a rotating wheel.* Sensors and Actuators a-Physical, 2010. **159**(2): p. 196-203.
47. Cottone, F., H. Vocca, and L. Gammaitoni, *Nonlinear Energy Harvesting.* Physical Review Letters, 2009. **102**(8).
48. Mitcheson, P.D., et al., *Tuning the Resonant Frequency and Damping of an Electromagnetic Energy Harvester Using Power Electronics.* Ieee Transactions on Circuits and Systems Ii-Express Briefs, 2011. **58**(12): p. 792-796.
49. Lau, S.L. and W.S. Zhang, *Nonlinear Vibrations of Piecewise-Linear Systems by Incremental Harmonic-Balance Method.* Journal of Applied Mechanics-Transactions of the Asme, 1992. **59**(1): p. 153-160.
50. Mockensturm, E.M. and R. Balaji, *Piece-wise linear dynamic systems with one-way clutches.* Journal of Vibration and Acoustics-Transactions of the Asme, 2005. **127**(5): p. 475-482.

51. Ding, H. and J.W. Zu, *Steady-State Responses of Pulley-Belt Systems With a One-Way Clutch and Belt Bending Stiffness.* Journal of Vibration and Acoustics-Transactions of the Asme, 2014. **136**(4).
52. Gill-Jeong, C., *Nonlinear behavior analysis of spur gear pairs with a one-way clutch.* Journal of Sound and Vibration, 2007. **304**(1-2): p. 18-30.
53. Zhu, F.R. and R.G. Parker, *Non-linear dynamics of a one-way clutch in belt-pulley systems.* Journal of Sound and Vibration, 2005. **279**(1-2): p. 285-308.
54. Zhu, F. and R.G. Parker, *Piece-wise linear dynamic analysis of serpentine belt drives with a one-way clutch.* Proceedings of the Institution of Mechanical Engineers Part C-Journal of Mechanical Engineering Science, 2008. **222**(7): p. 1165-1176.
55. Li, Z.J., et al., *Energy-harvesting shock absorber with a mechanical motion rectifier.* Smart Materials and Structures, 2013. **22**(2).
56. Orazov, B., O.M. O'Reilly, and O. Savas, *On the dynamics of a novel ocean wave energy converter.* Journal of Sound and Vibration, 2010. **329**(24): p. 5058-5069.
57. Diamond, C.A., O.M. O'Reilly, and O. Savas, *The impulsive effects of momentum transfer on the dynamics of a novel ocean wave energy converter.* Journal of Sound and Vibration, 2013. **332**(21): p. 5559-5565.
58. wireless, L., *GPS 6000 Series wildlife collars.* http://www.lotek.com/gps6000.htm.
59. ZyMOS, *Solar cell current-voltage curve with the max power point indicated.* Wikimedia, http://commons.wikimedia.org/wiki/File:Solar-Cell-IV-curve-with-MPP.png, 2006.
60. Park, C. and P.H. Chou., *Ambimax: Autonomous energy harvesting platform for multi-supply wireless sensor nodes.* Sensor and Ad Hoc Communications and Networks, 2006.
61. Nelson, C. and J. Williams, *LT1070 Design Manual.* Linear, http://cds.linear.com/docs/en/application-note/an19fc.pdf, 1986.
62. Cao, X.P., et al., *Electromagnetic energy harvesting circuit with feedforward and feedback DC-DC PWM boost converter for vibration power generator system.* Ieee Transactions on Power Electronics, 2007. **22**(2): p. 679-685.
63. Circuits, A.A., *Rectifier circuits.* http://www.allaboutcircuits.com/vol_3/chpt_3/4.html.
64. RENOLD, *Trapped Roller Clutches.* http://www.renold.com/Products/TrappedRollerFreewheels/TrappedRollerFreewheels.asp.
65. Matlab, *DC Motor Position: Simulink Modeling.* http://ctms.engin.umich.edu/CTMS/index.php?example=MotorPosition&section=SimulinkModeling.
66. Liang, C., Y. Wu, and L. Zuo, *vibration energy harvesting system with mechanical motion rectifier.* ASME 2015 Dynamic Systems and Control Conference, 2015.